nature communications

Article

https://doi.org/10.1038/s41467-026-68376-6

Near-infrared light-driven nanomotors-based microneedles for the active therapy of bacterial infected acne

Received: 10 March 2025

Accepted: 30 December 2025

Published online: 16 January 2026

Check for updates

Ziwei Hu[1,4], Yuyang Gan[2,4], Yiying Song[1], Hanfeng Qin[1], Limeng Liu[2], Lu Liu[1], Fei Peng[3] ✉, Zhexiang Fan[2] ✉ & Yingfeng Tu[1] ✉

Acne, caused by *Cutibacterium acnes*, triggers inflammatory lesions. The hypoxic biofilm microenvironment exacerbates acne progression, while inadequate hydrogen peroxide and dense biofilm barriers hinder oxygen generation and nanomedicine penetration. Here, we develop microneedles patch loaded with near infrared-driven self-oxygenating Z@P-M nanomotors for photothermal therapy of acne. Zinc peroxide nanoparticles are asymmetrically modified with polydopamine, followed by in-situ manganese dioxide growth on polydopamine to form Z@P-M nanomotors. Z@P-M nanomotors loaded microneedles penetrate the stratum corneum to deliver antibacterial nanoparticles into the dermis. In female murine acne, Zinc peroxide slowly releases hydrogen peroxide in acidic biofilm, catalyzed by manganese dioxide to generate oxygen, thus alleviating hypoxia and skin inflammation. After near infrared laser irradiation, the thermal gradient generated by the asymmetrically modified polydopamine coating endows the nanomotors with enhanced diffusion to promote biofilm penetration, further improving photothermal therapy efficacy and showing a potential for active acne treatment.

Acne is a common skin disease with the highest prevalence between the ages of 15 and 20. The erythematous lesions and scarring caused by acne have a profoundly negative impact on the emotional and mental health of adolescents[1,2]. In general, the anaerobic *Cutibacterium acnes* (*C. acnes*) are the main cause of acne. *C. acnes* can proliferate and release lipase, which decompose the accumulated sebum and produce free fatty acids, resulting in hypoxia, and eventually stimulating the secretion of pro-inflammatory factors from the skin cells, such as tumor necrosis factor-alpha (TNF-α) and interleukins (ILs)[3–5]. Moreover, skin-resident innate lymphoid cells (ILCs) participate in the regulation and maintenance of skin microbial homeostasis[6]. In particular, the reduction of retinoic acid receptor-related orphan receptor gamma t (RORγt$^+$) ILCs leads to an abnormal proliferation of sebaceous glands and increases sebum secretion, which is remarkably similar to the acne phenotype as well as to the adaptive survival environment of *C. acnes*[7]. Interestingly, bacterial extracellular vesicles (bEVs) of *C. acnes* can significantly reduce the amount of the skin ILCs, which may suggest that excessive accumulation of *C. acnes* could disrupt the homeostatic balance of skin-resident ILCs, thus leading to inflammatory skin lesions[8]. Therefore, developing a new strategy to alleviate hypoxia and inflammation induced by *C. acnes* infection and to restore the homeostasis of ILCs is significant for acne treatment. In clinic, mild or moderate acne cases are generally treated with topical medications, while moderate or severe acne cases are treated with oral antibiotics. However, frequent administration of antibiotics can result in severe side effects[2,9]. Moreover, biofilm formation by *C. acnes* is generally resistant to conventional antibiotics due to the protective effect of extracellular polymeric substances (EPS) of *C. acnes* biofilm[4].

[1]NMPA Key Laboratory for Research and Evaluation of Drug Metabolism & Guangdong Provincial Key Laboratory of New Drug Screening, School of Pharmaceutical Sciences, Southern Medical University, Guangzhou, China. [2]Department of Plastic and Aesthetic Surgery, Nanfang Hospital, Southern Medical University, Guangzhou, China. [3]School of Materials Science and Engineering, Sun Yat-Sen University, Guangzhou, China. [4]These authors contributed equally: Ziwei Hu, Yuyang Gan. ✉e-mail: pengf26@mail.sysu.edu.cn; zhexiang1990@smu.edu.cn; tuyingfeng1@smu.edu.cn

Consequently, localized application of antimicrobial agents directly offers a promising therapeutic strategy for combating acne formation. Microneedles (MNs) systems have the advantage of high transdermal efficiency, favorable patient compliance, and low frequency of drug delivery[10,11]. Nanoparticles (NPs) loaded MNs can penetrate easily into the stratum corneum and subsequently deliver antibacterial nanomedicines to the dermis for the treatment of acnes[12]. However, dense EPS in bacterial biofilm further prevents the penetration of antibacterial materials and reduces the therapeutic efficacy compared to pelagic bacteria[13]. Photothermal therapy (PTT) is non-invasive, highly controllable and wide-spectrum bactericidal. Biocompatible photothermal agents (PTAs) such as polydopamine (PDA) can convert light into thermal energy, thereby generating high temperature that dissociates the dense structure of the biofilm and leads to bacterial death, showing great potential in treating drug-resistant bacteria and eradicating biofilms[14,15]. However, photothermal NPs still have limited penetration in bacterial biofilms, which hinders the therapeutic efficacy of PTT[13].

Self-propelled nanomotors can overcome these drawbacks by converting external energies such as chemical reaction, light, magnetic field, or ultrasound into mechanical motion, which demonstrate significant potential in biomedicine for applications like targeted drug delivery and constructing mechanical-antibiofilm systems[16–19], especially near-infrared (NIR) light-driven nanomotors have aroused increasingly widespread research interest in eradicating bacterial biofilms[20]. Under 808 nm NIR laser irradiation, nanomotor generates a thermal gradient thereby triggering the self-thermophoresis, leading the nanomotor to propel in the direction opposite to the temperature gradient[21], which endows the nanomotor with a strong power to penetrate the biofilm. Although biofilm-infected tissues show relatively higher concentration of hydrogen peroxide (H_2O_2) compared to normal tissues, the concentration of H_2O_2 in the biofilm microenvironment is still insufficient to maintain a continuous supply of oxygen (O_2)[22]. Therefore, it is necessary to selectively increase the level of H_2O_2 in the biofilm, and converts them into O_2 to alleviate hypoxia of biofilm microenvironment. Zinc peroxide (ZnO_2) can degrade slowly and continuously in an acidic microenvironment and produce large amounts of H_2O_2[23], which provides sufficient fuel for oxygen production. With the development of nanotechnology, manganese dioxide (MnO_2) with catalase (CAT) mimetic activity is one of the most promising nanozymes. It can effectively catalyze the continuous supply of O_2 from microenvironmental H_2O_2, alleviating hypoxia and oxidative stress to reduce inflammatory responses[24]. Therefore, it is essential to design and fabricate oxygen self-supplying and self-thermophoretic nanomotors to overcome the biofilm barriers and alleviate hypoxia for active acne treatment.

Herein, we present an intelligent design of MNs encasing self-thermophoretic nanomotors driven by 808 nm NIR laser to alleviate hypoxia and eradicate biofilms for active acne treatment. Precise asymmetric regulation of Janus nanomotors enables the integration of materials with different functions into the single system, which is the basis for the self-propelled behavior of the nanomotor. Janus nanomotors are synthesized by asymmetrically wrapping photothermal PDA onto ZnO_2 (Z), following by MnO_2 growing on PDA in situ. The resulting nanomotors are then loaded into sodium hyaluronate MNs, here referred to Z@P-M MNs (Fig. 1). Upon pressing onto the skin, Z@P-M MNs are dissolved rapidly to release Z@P-M nanomotors in dermis. Asymmetrically grown PDA absorbs 808 nm NIR laser to generate a thermal gradient to induce self-thermophoresis, which endows the nanomotor with enhanced diffusion to penetrate the dense bacterial biofilm. The released Z@P-M nanomotors produce excess H_2O_2 in the acidic biofilm microenvironment and continuously supplies oxygen catalyzed by MnO_2, which not only alleviates the biofilm hypoxia and reduces inflammation, but also synergizes with PTT effect to eliminate the *C. acnes* biofilm, thereby restoring the ILCs homeostasis of acne.

Results

Fabrication and characterization of Z@P-M MNs and Z@P-M nanomotors

As shown in Fig. 1, ZnO_2 NPs were first synthesized via a simple one-pot method. Briefly, zinc chloride ($ZnCl_2$), poly (viny pyrrolidone) (PVP), and ammonia were dispersed in anhydrous ethanol, and hydrogen peroxide was then slowly added to form monodisperse ZnO_2. By regulating the interfacial energy difference[25], polyacrylic acid (PAA) network was asymmetrically wrapped on ZnO_2 to synthesis ZnO_2@PAA (Z@PAA), followed by PDA formation on PAA via dopamine hydrochloric polymerization to obtain Janus ZnO_2@PDA NPs (Z@P). The oxidation of potassium permanganate ($KMnO_4$) was then utilized to grow MnO_2 in situ on the PDA layer, referred as ZnO_2@PDA-MnO_2 (Z@P-M) nanomotors. To fabricate MNs, sodium hyaluronate with favorable biocompatibility and solubility was selected as raw materials. Hyaluronic acid (HA) is a natural polysaccharide, and can maintain skin moisture and promote skin absorption[4]. Therefore, sodium hyaluronate solution containing Z@P-M nanomotors was filled into the mold, vacuumed, dried and demolded to obtain Z@P-M MNs. As shown in Fig. 2a, b and Supplementary Fig. 1, The Z@P-M MNs patch size is 15 mm × 15 mm, featuring a grid of 225 MNs arranged in a uniform pattern. Scanning electron microscope (SEM) mapping images showed the elemental distribution of C, N, O, Zn, and Mn, indicating that Z@P-M was homogeneously distributed in sodium hyaluronate. Each MN stood at 637 μm in height, a dimension sufficient to traverse both the stratum corneum and epidermal layers (~100 μm) for targeted delivery to the dermal tissue[26]. The diameter of MN tip was 28.19 μm and this size also ensured the sufficient pressure for the skin penetration[27]. Sufficient mechanical strength is also important for MNs to penetrate the skin. In Fig. 2c and Supplementary Fig. 2, the stress-strain behavior of each MN was derived from the real-time monitoring of displacement-force variations during mechanical testing. A gradual increase in mechanical strength was clearly observed when sodium hyaluronate concentration was increased from 50 mg/mL to 150 mg/mL, and the compressive force of each MN at the 600 μm displacement was increased from 0.12 N to 0.26 N. In addition, the mechanical strength also gradually increased with increasing concentration of Z@P-M (ZnO_2 concentration = 50 − 100 μg/mL). The curve of Z@P-M MNs showed a continuous rising trend and the stress load was much larger than the minimum mechanical force required for MNs to penetrate the skin (0.098 N per needle)[28]. MNs did not fracture during the compression, indicating that the patch had sufficient mechanical strength to penetrate the skin. In addition, the water absorption of MNs patch in a humid environment (70 % humidity) was also evaluated. The needle gradually absorbed water and eventually dissolved within 30 min (Supplementary Fig. 3). The results indicated that the MNs patch has promising hygroscopic properties and can provide a favorable environment for tissue repair.

For the characterization of the loaded Z@P-M, transmission electron microscopy (TEM) images showed that asymmetric PDA and MnO_2 layers were clearly observed on one side of ZnO_2. Energy-dispersive X-ray spectroscopy (EDS) mapping further determined the elemental composition of Z@P-M. It was noteworthy that Zn was highly concentrated in the center, and C, N, and Mn were asymmetrically wrapped around Zn, demonstrating the asymmetric structure of MnO_2-modified PDA shell (Fig. 2d, and Supplementary Fig. 4). The spherical ZnO_2 particles were distributed uniformly with a particle diameter of 167.00 nm. When PDA layer was modified, the particle diameter increased to 221.82 nm, and the zeta potential also changed from 1.62 ± 0.08 mV to -13.27 ± 0.31 mV. After the successful deposition of MnO_2 on the surface of PDA, the particle diameter and zeta potential were 240.87 nm and -8.21 ± 0.06 mV, respectively (Fig. 2e, f). In addition, the diameters of Z@P-M before and after 808 nm NIR irradiation (1 W/cm^2, 5 min) were 242.03 ± 1.89 nm and 240.90 ± 0.40 nm, respectively, and the zeta potentials were

https://doi.org/10.1038/s41467-026-68376-6

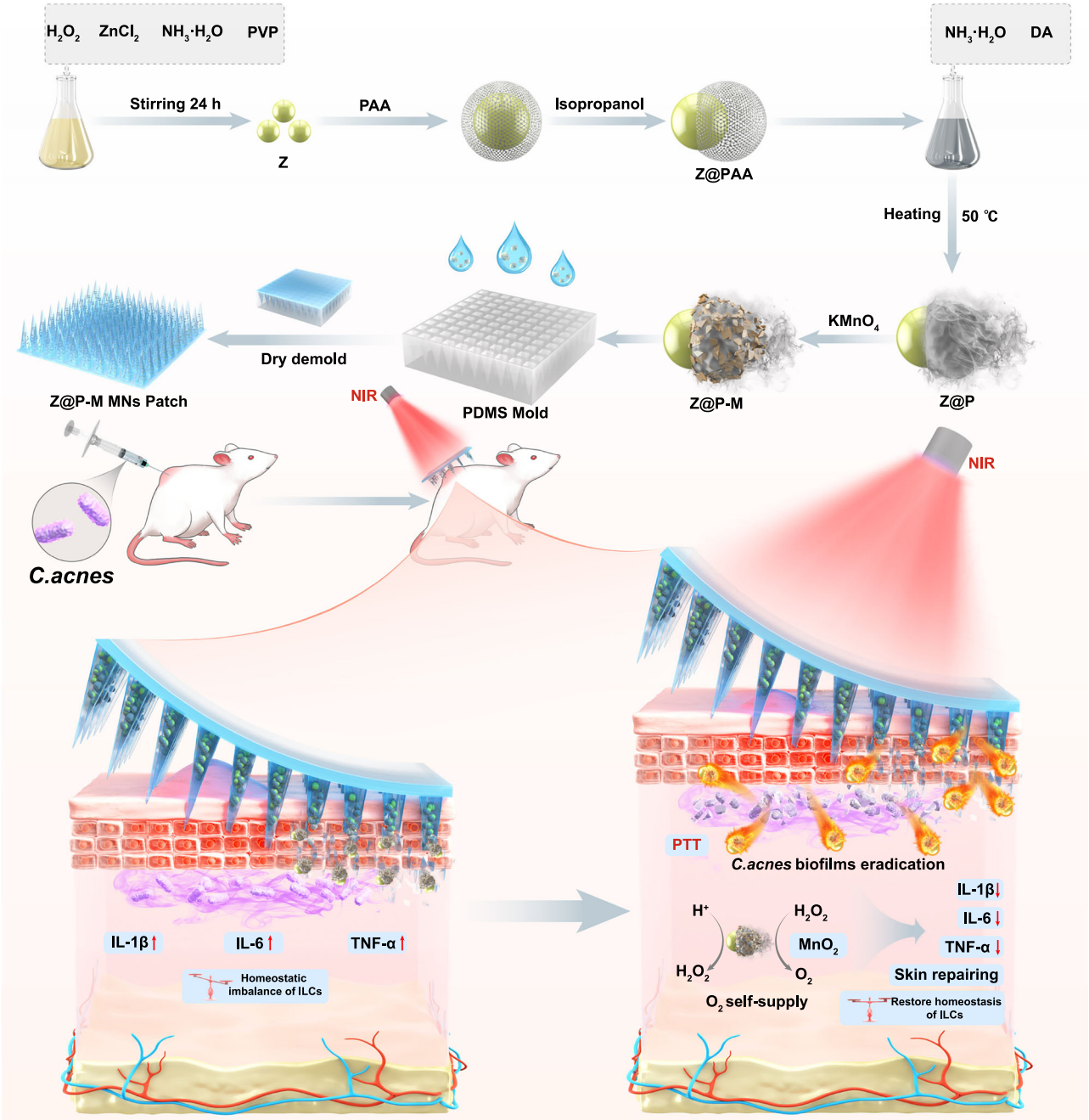

Fig. 1 | Fabrication of Z@P-M MNs and the active treatment of acne. Z@P-M MNs were dissolved and the loaded Z@P-M nanomotors were rapidly released in the dermis. The asymmetrically grown PDA absorbed 808 nm NIR light to generate self-thermophoresis, which allowed motion-promoted enhanced penetration of dense bacterial biofilms. The released Z@P-M nanomotors generated excess H_2O_2 in the acidic biofilm microenvironment and sustained oxygenation catalyzed by MnO_2, which not only alleviated biofilm hypoxia and reduced inflammation, but also cleared *C. acnes* biofilm synergistically with the PTT effect, thus restoring the homeostasis of ILCs in acne.

-8.49 ± 0.22 mV and -8.42 ± 0.07 mV, respectively, which was almost similar. TEM images exhibited no obvious degradation of Z@P-M before and after 808 nm NIR irradiation, and still maintained the Janus structure, indicating that Z@P-M kept structural stability (Supplementary Fig. 5). Raman spectra of ZnO_2 and ZnO were showed in Supplementary Fig. 6, where ZnO was the control. It was observed that the characteristic peak of ZnO was observed around 437 cm^{-1}, associating with the E_2 vibrational modes of O atoms. While the characteristic peak of ZnO_2 was around 840 cm^{-1}, which belonged to the O-O bond stretching band of the peroxide ion[29,30]. The above results indicated that ZnO_2 was successfully synthesized. Supplementary Fig. 7 showed the Fourier transform infrared spectrometer (FTIR) analysis of Z, Z@P, and Z@P-M. Z, Z@P, and Z@P-M exhibited an infrared absorption band at 1420 cm^{-1}, attributed to the vibrational mode of peroxide ions[31]. The FTIR spectrum of Z showed a sharp absorption band at 440 cm^{-1}, matching the Zn-O vibration band[32,33], confirming the successful synthesis of ZnO_2. Z@P and Z@P-M exhibited absorption peaks at 1595 cm^{-1}, corresponding to the C=O bond of PDA[34]. Z@P-M showed an absorption peak at 538 cm^{-1} corresponding to the Mn-O bond in MnO_2[35]. Figure 2g presented the X-ray Powder diffractometer (XRD) pattern of Z, Z@P, and Z@P-M. The yellow and blue lines represented Z and Z@P, respectively, which matched the

https://doi.org/10.1038/s41467-026-68376-6

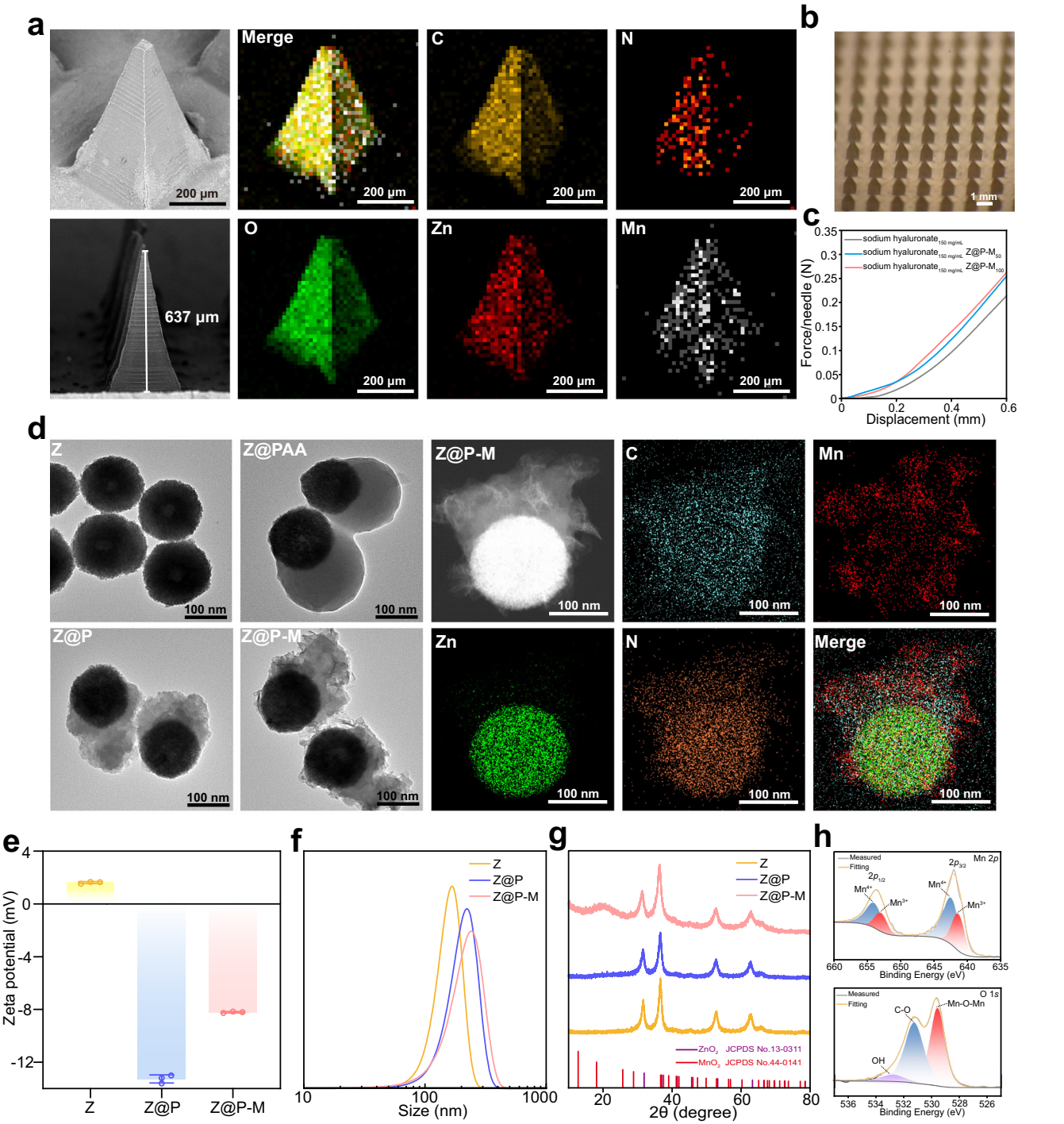

Fig. 2 | Fabrication and characterization of Z@P-M MNs. a SEM images and EDS mapping of Z@P-M MNs (scale bar = 200 μm). $n = 3$ independent experiments. **b** Optical image of Z@P-M MNs (scale bar = 1 mm). **c** Mechanical properties of MNs patches with and without different concentrations of Z@P-M (ZnO_2 concentration = 50 − 100 μg/mL) containing sodium hyaluronate concentration of 150 mg/mL. **d** TEM images of Z, Z@PAA, Z@P, and Z@P-M, and the corresponding EDS elemental mapping of Z@P-M (scale bar = 100 nm). $n = 3$ independent experiments. **e** Zeta potential of Z, Z@P, and Z@P-M. $n = 3$ independent experiments. **f** Diameter distribution of Z, Z@P, and Z@P-M. **g** XRD of Z, Z@P, and Z@P-M. JCPDS cards of ZnO_2 (No. 13-0311) and MnO_2 (No. 44-0141) were provided for comparison. **h** Mn 2*p* and O 1*s* XPS spectra of Z@P-M. Data in (**e**) were presented as Mean ± SD. Source data are provided as a Source Data file.

joint committee on powder diffraction standards (JCPDS) card of ZnO_2. The pink line represented Z@P-M, showing a diffraction peak at 18.75°, corresponding to (200) of MnO_2 crystallographic faces. In addition, the pattern of Z@P-M showed diffraction peaks at 31.38° and 62.86°, corresponding to (111) and (311) of ZnO_2 crystallographic faces, indicating that Z@P-M was successfully synthesized and ZnO_2 exhibited no apparent degradation during the synthesis of Z@P-M. C, N, O, Zn, and Mn of Z@P-M were further investigated by X-ray photoelectron spectroscopy (XPS), with elemental contents of 43.11 %, 2.83 %, 37.83 %, 6.36 %, and 9.87 %, respectively (Supplementary Fig. 8). The peaks at 642.08 eV and 653.68 eV corresponded to the Mn $2p_{3/2}$ and Mn $2p_{1/2}$ spin-orbit peaks of MnO_2, respectively. The Mn $2p_{3/2}$ and $2p_{1/2}$ spectra were each divided into two characteristic peaks, with those at 641.58 eV and 653.18 eV corresponding to Mn^{3+}, and those at 642.68 eV

https://doi.org/10.1038/s41467-026-68376-6

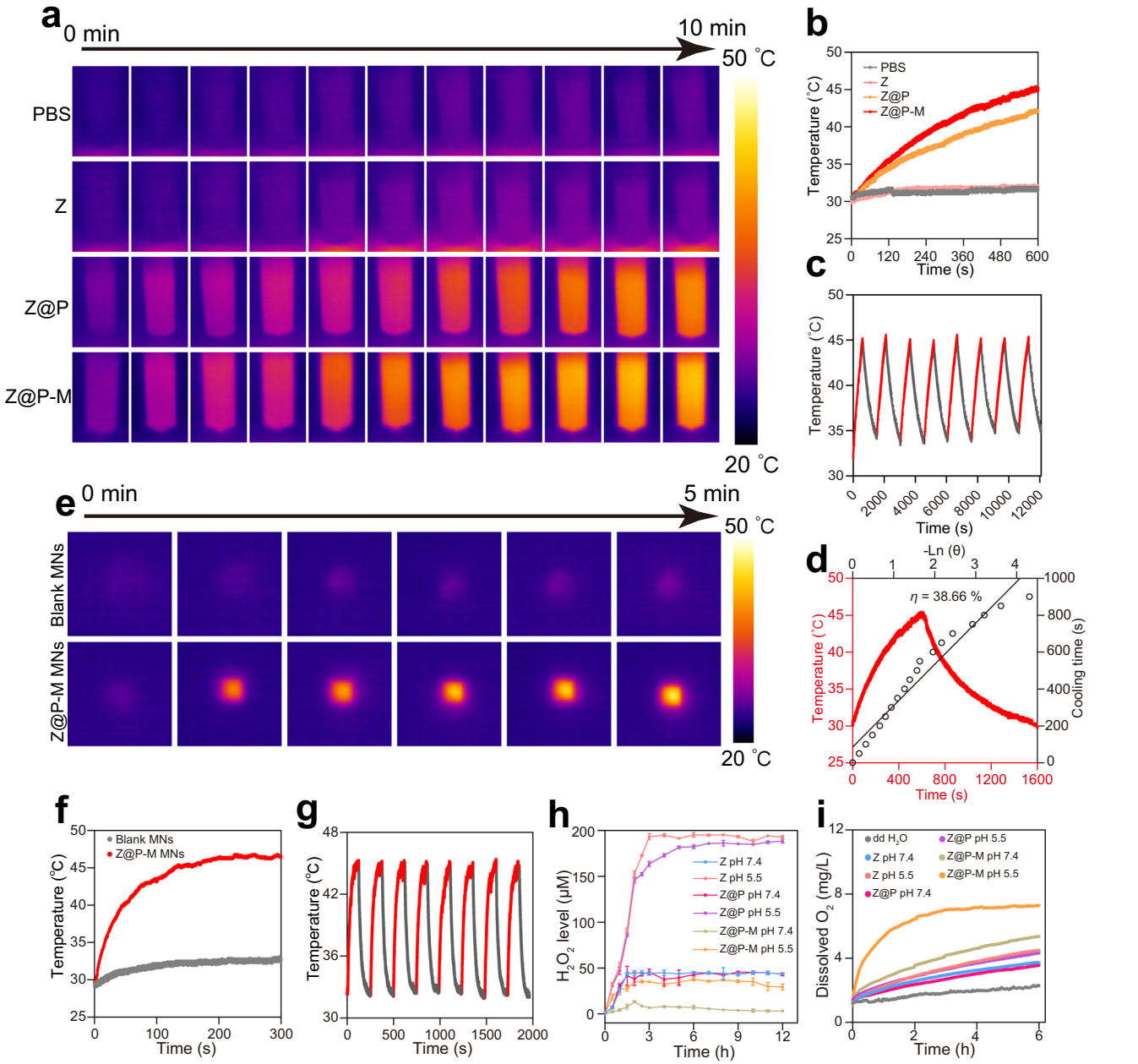

Fig. 3 | Photothermal capabilities and acidic release of Z@P-M and Z@P-M MNs. IR photothermal images (**a**) and temperature increase curves (**b**) of PBS, Z, Z@P, and Z@P-M under 10 min of 1 W/cm^2 808 nm NIR irradiation. **c** 8 heating/cooling cycles of Z@P-M suspension (ZnO_2 concentration = 100 μg/mL) under 1 W/cm^2 808 nm NIR irradiation. **d** Photothermal conversion efficiency of Z@P-M. IR photothermal images (**e**) and temperature increase curves (**f**) of blank MNs and Z@P-M MNs under 5 min of 1 W/cm^2 808 nm NIR irradiation. **g** 8 heating/cooling cycles of Z@P-M MNs under 1 W/cm^2 808 nm NIR irradiation. H_2O_2 (**h**) and O_2 (**i**) release profiles of Z, Z@P, and Z@P-M under pH 7.4 and 5.5. $n = 3$ independent experiments. Data in (**h**) was presented as Mean ± SD. Source data are provided as a Source Data file.

and 654.28 eV corresponding to Mn^{4+}[36]. The peaks in the O 1*s* spectrum mainly belonged to the O-H bond (532.78 eV), C-O (531.28 eV), and Mn-O-Mn bond (529.58 eV)[37], thus confirming the presence of MnO_2 in Z@P-M, consistent with the XRD and FTIR results (Fig. 2h).

After successful fabrication of Z@P-M, the photothermal properties were then evaluated by real-time infrared (IR) thermal camera. As shown in Fig. 3a, the IR photothermal images presented a clear temperature difference between PBS, Z, Z@P, and Z@P-M during 10 min of 1 W/cm^2 808 nm NIR irradiation, which was consistent with the photothermal curves shown in Fig. 3b. After 10 min of 1 W/cm^2 808 nm NIR irradiation, the temperatures of Z, Z@P, and Z@P-M were increased to 32.1 °C, 42.1 °C, and 45 °C, respectively, while the PBS group only increased by 0.8 °C. It was notable that under the same 808 nm NIR irradiation (10 min, 1 W/cm^2), Z@P-M exhibits better photothermal effects compared to Z@P. It was attributed to Z@P-M combining PDA and MnO_2, two excellent photothermal agents, thereby exhibiting a significant cumulative photothermal effect[38]. Z@P-M with 100 μg/mL of ZnO_2 concentration was also irradiated with 808 nm NIR laser with different intensities for 10 min (0.5, 1, and 1.5 W/cm^2), and the temperatures were increased to 35.8 °C, 45.1 °C and 51.2 °C, respectively (Supplementary Fig. 9a). When the 808 nm NIR power of 1 W/cm^2 was applied for 10 min, the temperatures increased sequentially (38.6 − 49.6 °C) with increasing concentrations of Z@P-M (ZnO_2 concentration = 50 − 200 μg/mL), indicating that the

photothermal effect of Z@P-M was proportional to the sample concentration (Supplementary Fig. 9b). In addition, Z@P-M presented almost consistent heating/cooling curves after 8 cycles of 808 nm NIR irradiation (1 W/cm^2) (Fig. 3c), which proved that Z@P-M had good photothermal stability. The photothermal conversion efficiency (η) of Z@P-M was also calculated, and the η value was 38.66 %, indicating that the developed Z@P-M was a potential photothermal agent (Fig. 3d). Moreover, the IR photothermal images and temperature rise curves of the MNs patches showed that Z@P-M MNs patch had favorable photothermal conversion properties under 1 W/cm^2 808 nm NIR irradiation for 10 min (Fig. 3e, f). Z@P-M MNs showed almost consistent heating/cooling curves after 8 cycles of 808 nm NIR irradiation (1 W/cm^2), illustrated that Z@P-M MNs patch could withstand prolonged laser irradiation with high photothermal stability (Fig. 3g).

The endogenous H_2O_2 concentration in biofilm-infected tissues is generally higher than that in normal tissues, but is still insufficient to trigger the rapid and efficient oxygen release[22]. Therefore, it is necessary to selectively increase the H_2O_2 level in the biofilm. Z@P-M nanomotor could release massive H_2O_2, and the H_2O_2 concentration at pH 5.5 and pH 7.4 was detected by a H_2O_2 detection kit. At pH 7.4, H_2O_2 release levels of Z and Z@P reached 43.38 ± 0.81 μM and 43.17 ± 1.59 μM during 12 h, respectively, indicating that ZnO_2 was decomposed slowly to produce H_2O_2 under neutral conditions (pH = 7.4). When the pH was 5.5, the H_2O_2 release levels of Z and Z@P within 12 h increased sharply to 192.58 ± 1.91 μM and 188.46 ± 2.43 μM, respectively, which were 343.94 ± 5.13 % and 336.82 ± 11.02 % higher than those under neutral condition (pH = 7.4). It was demonstrated that H_2O_2 in the suspension mainly originated from the acid decomposition of ZnO_2, and the modification of PDA barely affected the H_2O_2 release levels. Under pH 7.4 and 5.5 conditions, the H_2O_2 levels of Z@P-M reached to 3.19 ± 0.76 μM and 29.26 ± 3.18 μM within 12 h, respectively. This significant difference in H_2O_2 concentration indicated that the MnO_2 from Z@P-M decomposed the generated H_2O_2, leading to a decrease in H_2O_2 levels in Z@P-M (Fig. 3h). Moreover, the O_2 release level of Z, Z@P, and Z@P-M were examined by dissolved oxygen analyzer. O_2 release levels of Z (pH 7.4), Z (pH 5.5), Z@P (pH 7.4), and Z@P (pH 5.5) within 6 h were 3.74 ± 0.10 mg/L, 4.49 ± 0.09 mg/L, 3.56 ± 0.29 mg/L, and 4.32 ± 0.23 mg/L, respectively. Their release levels were all higher than those of the control group (dd H_2O, 2.28 ± 0.07 mg/L), attributed to the slow decomposition of H_2O_2 from Z and Z@P at room temperature. Compared with Z@P, Z@P-M showed increased levels of O_2 release under neutral and acidic conditions, reaching 5.37 ± 0.44 mg/L and 7.31 ± 0.14 mg/L, respectively. These results suggested that MnO_2 from Z@P-M catalyzed the generated H_2O_2, thereby continuously producing O_2. The microenvironment of bacterial biofilms is generally acidic (pH = 4.5 − 6.5) and hypoxic[39,40]. Therefore, acid-responsive ZnO_2 could supply a large amount of H_2O_2 via acid decomposition in biofilm microenvironment. The produced H_2O_2 can be further catalyzed by MnO_2 to generate O_2, thereby alleviating hypoxia of biofilm and reducing inflammation[41] (Fig. 3i). Similarly, the release rate of Zn^{2+} under acidic condition (pH 5.5) was 86.55 ± 7.14 % during 24 h, which was significantly higher than that under pH 7.4 (Supplementary Fig. 10). The results demonstrated that Z@P-M could be degraded under acidic condition, effectively releasing Zn^{2+} and O_2.

Z@P-M with enhanced diffusion promotes skin tissues and biofilm penetration

The asymmetric distribution of PDA-MnO_2 shell in Z@P-M nanomotors leads to asymmetric absorption of 808 nm NIR laser, thus generating a temperature gradient that produces self-thermophoresis for the actuation of the nanomotors[42]. The motion of Z@P-M in PBS under 808 nm NIR irradiation (0, 0.5, 1, and 1.5 W/cm^2) was recorded by inverted optical microscopy, and the motion trajectories were analyzed subsequently using Image J. As shown in Fig. 4a and Supplementary movie 1, enhanced diffusion of Z@P-M nanomotors was clearly observed with lengthened trajectories with the gradual increase of 808 nm NIR powers (0 − 1.5 W/cm^2). Under 808 nm NIR irradiation (0 − 1.5 W/cm^2), the motion of Z@P-M was positively correlated with the 808 nm NIR power. Z@P-M showed classical Brownian motion without 808 nm NIR irradiation. Under 1.5 W/cm^2 808 nm NIR irradiation, the velocity of Z@P-M was 4.16 ± 0.26 μm/s, which was 1.42 ± 0.07 folds higher than that of Brownian motion (2.94 ± 0.25 μm/s) (Fig. 4b). The diffusion of NIR light-driven nanomotors was further investigated by mean-square displacement (MSD) analysis. The MSD exhibited an increase proportional to laser intensity escalation (0 − 1.5 W/cm^2), indicating enhanced propulsion capacity of Z@P-M nanomotors (Fig. 4c). The enhanced diffusion of Z@P-M nanomotors actuated by 808 nm NIR laser further provided the basis for skin tissues and biofilm penetration.

To verify the dissolution and penetration of Z@P-M MNs patches in the skin, a penetration experiment was performed by porcine skin with similar structure to human skin[43]. Z@P-M MNs patches were pressed onto the porcine skin for 5 min, followed by 808 nm NIR irradiation (1 W/cm^2) for 5 min. After the treatment, the patches were carefully removed. As shown in Supplementary Fig. 11, MNs on the patches were completely dissolved during the 10-min treatment, indicating that Z@P-M MNs exhibited favorable skin solubility. To further investigate the dynamic dissolution and penetration process of Z@P-M MNs in the skin, Z@P-M was labelled with Rhodamine B (RhB) and loaded in the MNs patches, and z-stack fluorescence images of the skin were captured by confocal laser scanning microscopy (CLSM). After inserting Z@P-M MNs patch into the skin for 5 min, strong fluorescence was observed within the 0 − 300 μm depth range. The patch was then exposed to 1 W/cm^2 808 nm NIR irradiation for 3 or 5 min. At 3 min of 1 W/cm^2 808 nm NIR irradiation, the fluorescence intensity in the 0 − 200 μm depth range decreased sharply, while the fluorescence intensity increased in the 400 − 500 μm depth range. At 5 min of 1 W/cm^2 808 nm NIR irradiation, the depth range of fluorescence further expanded to 400 − 600 μm, confirming that Z@P-M exhibited enhanced permeability in the skin under 1 W/cm^2 808 nm NIR irradiation. This was attributed to the effective motility caused by self-thermophoresis of Z@P-M, thereby enhancing deep penetration in skin tissues (Fig. 4d, and Supplementary Fig. 12).

In order to demonstrate the effect of the asymmetric structure on penetration, ZnO_2#PDA-MnO_2 (Z#P-M) NPs were also developed by encapsulating ZnO_2 with PDA-MnO_2 layer completely. The penetration efficiency of Z@P-M and Z#P-M NPs into *methicillin-resistant staphylococcus aureus* (*MRSA*) and *C. acnes* biofilms was investigated by scanning with CLSM, where Z@P-M and Z#P-M NPs were labelled with RhB (red). Without 808 nm NIR irradiation, Z@P-M and Z#P-M NPs stayed on the surface of the *C. acnes* biofilm and the penetration was significantly delayed. Whereas, the penetration of Z@P-M and Z#P-M NPs into the biofilm was notably observed under 5 min of 1 W/cm^2 808 nm NIR irradiation (Fig. 4e, and Supplementary Fig. 13a). The red fluorescence intensity of each cross-section was analyzed by Image J (Fig. 4f, and Supplementary Fig. 13b). Under 1 W/cm^2 808 nm NIR irradiation, Z@P-M had maximum fluorescence intensity at 10 μm and 8 μm depths in *MRSA* and *C. acnes* biofilms respectively, while the maximum fluorescence intensity of Z#P-M in both biofilms was stopped at 6 μm. Later, the fluorescence intensity of the biofilm sections (0 − 20 μm) was further analyzed. At the lowest bottom (20 μm) and under 1 W/cm^2 808 nm NIR irradiation, the Z@P-M fluorescence intensity of *MRSA* and *C. acnes* biofilms were 13.08 ± 3.70 and 3.61 ± 0.09 folds higher than that of Z#P-M, which indicated that NIR light-actuated Z@P-M nanomotors could penetrate the biofilms efficiently.

https://doi.org/10.1038/s41467-026-68376-6

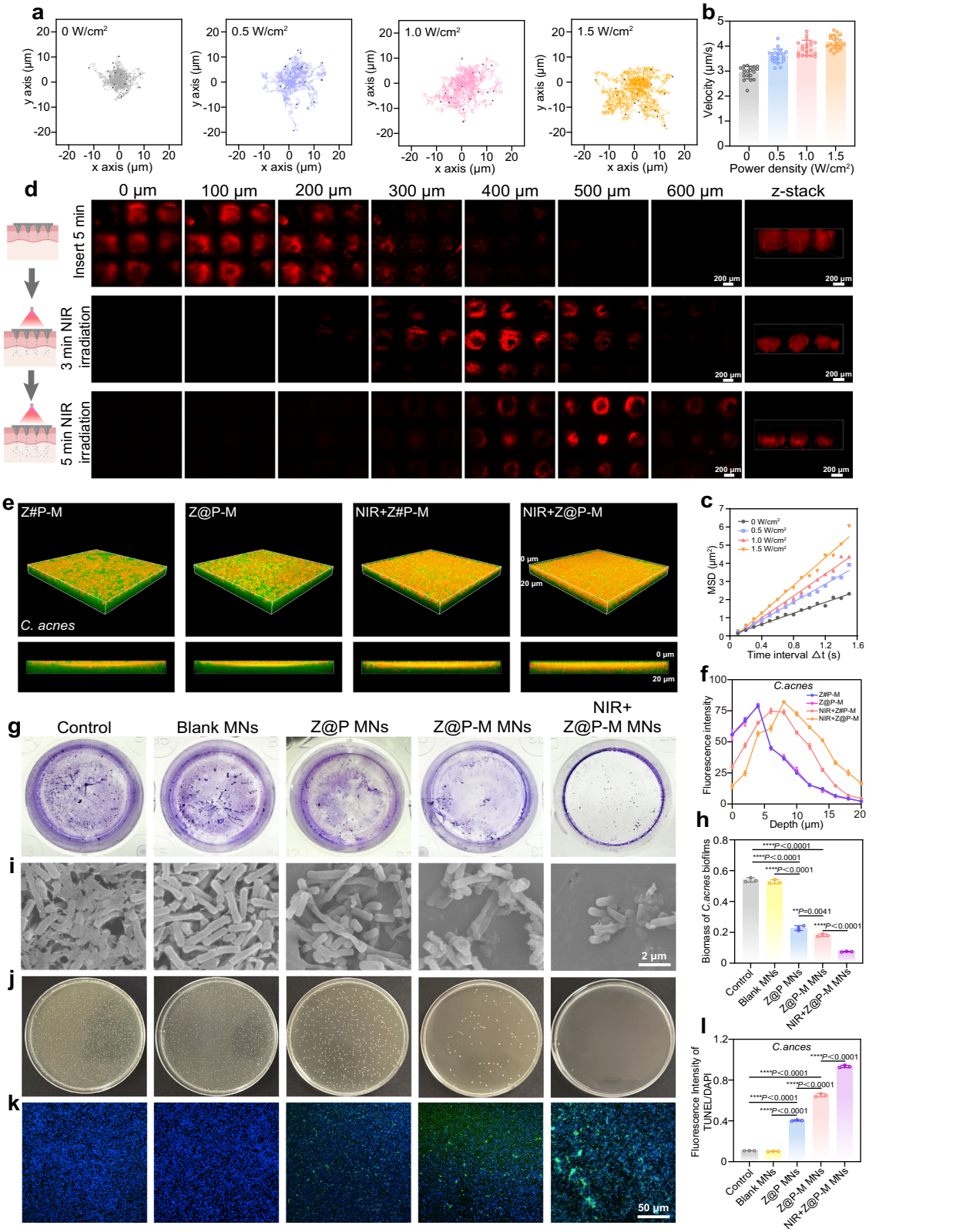

Antibacterial, antibiofilm and antiinflammation evaluation of Z@P-M MNs

C. acnes infections are the main source of acne, and antibiotic therapy is now the primary treatment for acne[4]. However, the misuse of antibiotics leads to potential drug resistance[44], so we selected *MRSA* and *C. acnes* as models for acne. A systematic anti-biofilm evaluation of NIR light-actuated Z@P-M MNs was carried out. 1 mL of bacterial suspension (1×10^8 CFU/mL) was seeded in 24-well plates for 48 h incubation to form mature biofilms. Figure 4g-h and Supplementary Fig. 14 showed the crystal violet (CV)-stained *C. acnes* and *MRSA* biofilms after incubation with Z@P-M MNs. CV staining showed that NIR + Z@P-M MNs group (5 min of 1 W/cm² 808 nm NIR irradiation) disrupted the biofilm most significantly, attributed to PTT effect and motility of NIR light-endowed Z@P-M nanomotor. Compared with the

Fig. 4 | Enhanced diffusion, penetration and antibiofilm effect of Z@P-M and Z@P-M MNs. Tracking trajectories (**a**) and velocity (**b**) of Z@P-M nanomotors under 30 s irradiation of different 808 nm NIR intensities (0, 0.5, 1, 1.5 W/cm^2). $n = 20$ independent experiments. **c** Average MSD calculated from the tracking trajectories under 30 s irradiation of different 808 nm NIR intensities (0, 0.5, 1, 1.5 W/cm^2) ($\Delta t = 1.5$ s). $n = 20$ independent experiments. **d** Fluorescence images of porcine skin treated with RhB labelled Z@P-M-loaded MNs patches at varied depths (0 − 600 μm) after Z@P-M MNs insertion and 808 nm NIR irradiation, where 1 W/cm^2 808 nm NIR irradiation was applied for 3 min or 5 min. $n = 3$ independent experiments (scale bar = 200 μm). Schematic diagram was created in BioRender by Hu, Z. (https://BioRender.com/wd2r0cf). **e** CLSM images of 5-CFDA - stained *C. acnes* biofilms after treating with RhB labelled Z@P-M and Z#P-M with or without 808 nm NIR irradiation, where 1 W/cm^2 808 nm NIR irradiation was applied for 5 min. The red and green fluorescence represented RhB-labeled NPs and 5-CFDA-stained *C. acnes* biofilms, respectively. $n = 3$ independent experiments. **f** Fluorescence intensity of RhB labelled Z@P-M and Z#P-M between 0 − 20 μm of section. $n = 3$ independent experiments. Crystalline violet staining of *C. acnes* biofilms (**g**) and biomass of *C. acnes* (**h**) after treating with PBS, blank MNs, Z@P MNs, Z@P-M MNs, and NIR + Z@P-M MNs, where 1 W/cm^2 808 nm NIR irradiation was applied for 5 min. $n = 3$ independent experiments. **i** SEM characterization of *C. acnes* biofilms structural modifications after different treatments (scale bar = 2 μm), where 1 W/cm^2 808 nm NIR irradiation was applied for 5 min. $n = 3$ independent experiments. **j** Representative photographs of *C. acnes* bacterial colonies after different treatments, where 1 W/cm^2 808 nm NIR irradiation was applied for 5 min. $n = 5$ independent experiments. TUNEL fluorescence images (**k**) and fluorescence quantification (**l**) of *C. acnes* after different treatments, where 1 W/cm^2 808 nm NIR irradiation was applied for 5 min. The green and blue fluorescence represented TUNEL and DAPI, respectively. $n = 3$ independent experiments (scale bar = 50 μm). Data in (**b**), (**f**), (**h**), and (**l**) were presented as Mean ± SD. *P* values in (**h**) and (**l**) were analyzed by one-way ANOVA with Tukey's multiple comparisons test (**$P < 0.01$, ****$P < 0.0001$). Source data are provided as a Source Data file.

blank MNs group, the biomass of *C. acnes* and *MRSA* biofilms in the Z@P MNs group decreased by 56.96 ± 2.09 % and 60.70 ± 1.34 %, respectively, suggesting that the H_2O_2 produced by Z@P MNs inhibited biofilm formation and antimicrobial activity to a certain extent. As reported, H_2O_2 with concentration of 10^{-5} − 10^{-4} M indeed inhibited bacterial and biofilms activity to some extent in vitro and in vivo, and H_2O_2 concentration as high as 166 mM − 1 M were necessary to achieve ideal antibacterial effects[45,46]. Biomass of *C. acnes* and *MRSA* biofilms in Z@P-M MNs group was decreased by 20.43 ± 2.21 % and 41.88 ± 3.11 % compared with that in Z@P MNs group, due to the O_2 release in response to acidic biofilm microenvironment inhibiting anaerobic *C. acnes*[47]. Moreover, the surface of Z@P-M was covered with MnO_2 nanosheets, which inhibited the formation of *C. acnes* and *MRSA* biofilms by inserting into bacteria to disrupt the cell membranes due to their extremely high aspect ratio edges[48]. Under 5 min of 1 W/cm^2 808 nm NIR irradiation, the biomass of *C. acnes* and *MRSA* biofilms was significantly reduced by 58.76 ± 0.69 % and 73.00 ± 0.72 % in the NIR + Z@P-M MNs group compared to that of the Z@P-M MNs group. Moreover, the effect of different exposure durations at 1 W/cm^2 808 nm NIR irradiation on biomass in the NIR + Z@P-M MNs group was also investigated. Compared with the Z@P-M MNs group, after 3 min and 5 min of 1 W/cm^2 808 nm NIR irradiation, the biomass of *C. acnes* biofilms decreased by 31.04 ± 4.64 % and 57.34 ± 3.41 %, respectively, while the biomass of *MRSA* biofilms decreased by 47.68 ± 0.58 % and 69.99 ± 0.36 % (Supplementary Fig. 15). It indicated that 5 min of 1 W/cm^2 808 nm NIR irradiation had the best anti-biofilm effect. In addition, SEM images showed that the group of Z@P MNs, Z@P-M MNs, and NIR + Z@P-M MNs exhibited some degree of damage to the bacterial structure. In particular, the NIR + Z@P-M MNs group (5 min of 1 W/cm^2 808 nm NIR irradiation) exhibited the most obvious bacterial structural distortion and collapse (Fig. 4i, Supplementary Fig. 16). Compared with the control group, TEM images of bacteria revealed that the membrane structure integrity of *C. acnes* and *MRSA* bacteria in the NIR + Z@P-M MNs group (5 min of 1 W/cm^2 808 nm NIR irradiation) was severely disrupted, accompanied by obvious cytoplasmic leakage (Supplementary Fig. 17). Standard plate counting showed the similar results (Fig. 4j, and Supplementary Fig. 18). Compared with the blank MNs group, the survival rates of *C. acnes* and *MRSA* were reduced in the Z@P MNs group and Z@P-M MNs group, indicating that Z@P MNs and Z@P-M MNs had antibacterial effects. After 5 min of 1 W/cm^2 808 nm NIR irradiation, the survival rates of *C. acnes* and *MRSA* in the NIR + Z@P-M MNs group were decreased to 0.09 ± 0.04 % and 0.59 ± 0.22 %, respectively. Compared with the Z@-M MNs group, 1 W/cm^2 808 nm NIR irradiation for 3 min and 5 min resulted in survival rates of *C. acnes* decreasing by 65.31 ± 7.01 % and 94.26 ± 1.41 %, respectively, while the survival rates of *MRSA* decreased by 53.45 ± 9.11 % and 94.53 ± 1.55 %, respectively (Supplementary Fig. 19), demonstrating that 1 W/cm^2 808 nm NIR irradiation for 5 min exhibited the optimal antibacterial effect. Terminal-deoxynucleotidyl transferase mediated nick end labeling (TUNEL) assay was also used to detect DNA damage in bacteria after different treatments. Compared with the blank MNs group, TUNEL fluorescence was enhanced in the Z@P MNs group, Z@P-M MNs group, and NIR + Z@P-M MNs group (5 min of 1 W/cm^2 808 nm NIR irradiation). Among these, the NIR + Z@P-M MNs group (5 min of 1 W/cm^2 808 nm NIR irradiation) exhibited the most intense TUNEL fluorescence, confirming that Z@P-M MNs can effectively damage bacterial DNA under 808 nm NIR light irradiation (Fig. 4k-l, Supplementary Fig. 20). It was suggested that the NIR light-driven Z@P-M nanomotor not only disrupted the bacterial structure via PTT effect, but also enhanced the diffusion and penetration in the biofilms due to the motility conferred by its Janus structure, which is promising for treating infections of drug-resistant bacterial biofilms in vivo.

We further investigated the therapeutic effects of Z@P-M MNs in vitro. The cytotoxicity of Z@P-M with different ZnO_2 concentrations was first evaluated by CCK-8 assay. As shown in Fig. 5a, Z@P-M with ZnO_2 concentration less than 100 μg/mL had no significant toxicity. To further explore the biocompatibility of different materials on NIH3T3 cells, HaCaT cells, and Raw 264.7 cells, calcein acetoxymethyl ester/propidium iodide (Calcein-AM/PI) was used to stain the live and dead cells, which showed green and red fluorescence, respectively (Fig. 5b, and Supplementary Fig. 21). Comparing with control group, no significant cytotoxicity of blank MNs, Z@P MNs, Z@P-M MNs, and NIR + Z@P-M MNs (5 min of 1 W/cm^2 808 nm NIR irradiation) was clearly observed in NIH3T3 cells, HaCaT cells, and Raw 264.7 cells, indicating that the synthesized MNs patches were indeed biocompatible. Cellular internalization was evaluated in NIH3T3 cells co-cultured with RhB-labelled Z@P-M MNs and Z#P-M MNs, followed by 5 min 808 nm NIR irradiation (1 W/cm^2). Cytoskeletal architecture was visualized using actin-tracker green fluorophore. Supplementary Fig. 22 showed that weak fluorescence was observed in the Z@P-M MNs group and Z#P-M MNs group without NIR light treatment. Under 5 min of 1 W/cm^2 808 nm NIR irradiation, the fluorescence intensity of the Z@P-M MNs group was 39.73 ± 13.06 % higher than that of the Z#P-M MNs group, indicating that NIR light-triggered enhanced diffusion promoted the cellular uptake of the released Z@P-M nanomotors, which supported a better therapeutic effect of the nanomotor in vitro.

To confirm the repairing effect of MNs patches on the infected tissues, scratching assay of NIH3T3 cells was performed in a hypoxia environment. In Fig. 5c,d, the migration rate of the Z@P MNs group increased to 52.05 ± 2.34 % and 70.92 ± 1.83 % at 18 and 36 h, respectively, which was higher than that of the blank MNs group. It was attributed to the fact that Zn^{2+} derived from ZnO_2 could promote fibroblast proliferation and migration, thereby promoting wound healing[4]. Compared with the Z@P MNs group, the migration rates of Z@P-M MNs group at 36 h increased by 13.03 ± 0.51 %, demonstrating that oxygen released from Z@P-M MNs under hypoxic conditions

https://doi.org/10.1038/s41467-026-68376-6

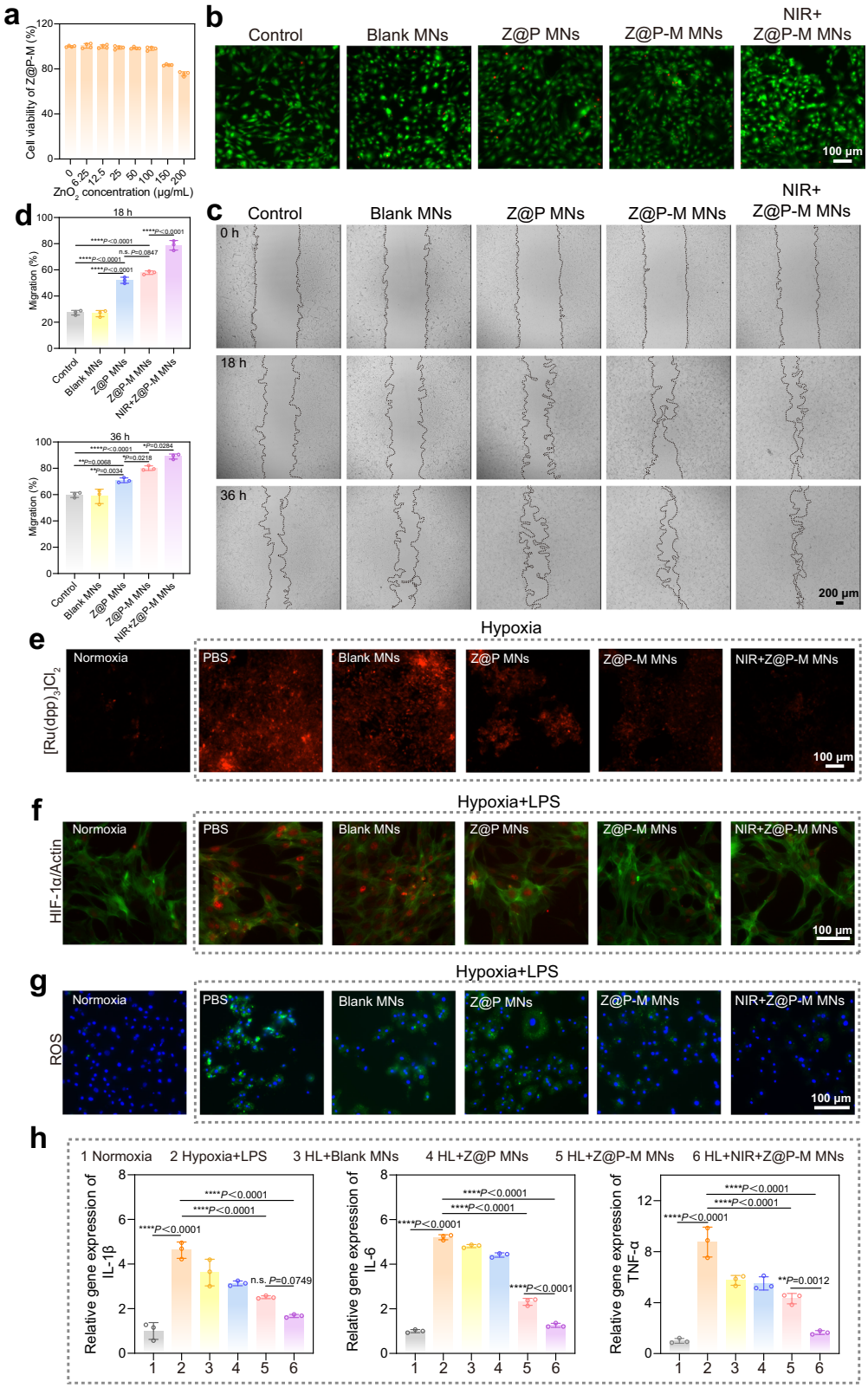

promoted the skin cell migration[49]. When compared with the Z@P-M MNs group, the migration rate at 18 h and 36 h further increased by 36.07 ± 3.23 % and 11.01 ± 1.47 % after 5 min of 1 W/cm^2 808 nm NIR irradiation, indicating that 808 nm NIR irradiation promoted the migration of fibroblasts. NIR light not only promoted the release of active Z@P-M nanomotors from MNs, but also improved the cell metabolism and regulated inflammatory responses, thereby accelerating the fibroblasts migration and the repair of the infected tissues[50]. The O_2 release level of Z@P-M MNs in vitro was further assessed by oxygen sensing probe [(Ru(dpp)$_3$)]Cl$_2$. As shown in Fig. 5e and Supplementary Fig. 23a, the probe fluorescence intensity of the Z@P-M MNs group was decreased by 60.64 ± 2.67 % compared with that of the Z@P MNs group. The fluorescence intensity of Z@P-M MNs was further decreased by 46.83 ± 3.47 % after 5 min of 1 W/cm^2 808 nm

Fig. 5 | Evaluation of Z@P-M MNs in vitro. a Cytotoxicity after treating with Z@P-M (ZnO_2 concentration: 0 − 200 μg/mL). $n = 4$ independent experiments. **b** Live/dead cells staining of NIH3T3 cells after different treatments, where 1 W/cm^2 808 nm NIR irradiation was applied for 5 min. The green fluorescence indicated live cells, and red fluorescence was dead cells (scale bar = 100 μm). $n = 3$ independent experiments. **c** Images of NIH3T3 cells scratch after different treatments, where 1 W/cm^2 808 nm NIR irradiation was applied for 5 min (scale bar = 200 μm). $n = 3$ independent experiments. **d** Migration rates of NIH3T3 cells after different treatments, where 1 W/cm^2 808 nm NIR irradiation was applied for 5 min. $n = 3$ independent experiments. **e** O_2 sensing probe $[(Ru(dpp)_3)]Cl_2$ staining of NIH3T3 cells after different treatments, where 1 W/cm^2 808 nm NIR irradiation was applied for 5 min (scale bar = 100 μm). $n = 3$ independent experiments. **f** HIF-1α fluorescence staining of NIH3T3 cells after different treatments, where 1 W/cm^2 808 nm NIR irradiation was applied for 5 min. The red and green fluorescence represented HIF-1α and actin, respectively (scale bar = 100 μm). $n = 3$ independent experiments. **g** ROS fluorescence staining of NIH3T3 cells after different treatments, where 1 W/cm^2 808 nm NIR irradiation was applied for 5 min. The green and blue fluorescence represented ROS and cell nucleus, respectively (scale bar = 100 μm). $n = 3$ independent experiments. **h** IL-1β, IL-6, and TNF-α gene expression in NIH3T3 cells after treating with (1) normoxia, (2) hypoxia + LPS (HL), (3) HL + blank MNs, (4) HL + Z@P MNs, (5) HL + Z@P-M MNs, (6) HL + NIR + Z@P-M MNs, where 1 W/cm^2 808 nm NIR irradiation was applied for 5 min. $n = 3$ independent experiments. Data in (**a**), (**d**), and (**h**) were presented as Mean ± SD. *P* values in (**d**) and (**h**) were analyzed by one-way ANOVA with Tukey's multiple comparisons test (n.s. represented no significance, $^*P < 0.05$, $^{**}P < 0.01$, $^{****}P < 0.0001$). Source data are provided as a Source Data file.

NIR irradiation. Hypoxia-Inducible Factor 1α (HIF-1α) was generally activated in hypoxic skin tissues, and its expression was decreased by continuous delivery of oxygen[51]. The enhanced diffusion of NIR light-actuated Z@P-M nanomotors promoted the accumulation of nanomotor into the cells[52], which enhanced cellular oxygen delivery and further reduced the expression of HIF-1α. Therefore, the oxygenation capacity of Z@P-M MNs was further confirmed by HIF-1α immunofluorescence in vitro. Lipopolysaccharide (LPS) and hypoxia successfully induced high HIF-1α expression in the cells, whereas Z@P-M MNs treatment with or without 808 nm NIR irradiation both showed decrease in HIF-1α expression, in which the most significant decrease in HIF-1α expression was observed for NIR + Z@P-M MNs group, where 1 W/cm^2 808 nm NIR irradiation was applied for 5 min (Fig. 5f, and Supplementary Fig. 23b). It was illustrated that the catalytic effect of the coated MnO_2 synergized with NIR light-actuated nanomotor enhanced diffusion to increase the continuous oxygen delivery. In general, improvement of hypoxia and scavenging of reactive oxygen species (ROS) can alleviate the inflammatory response of biofilm infection[53]. As expected, NIH3T3 cells showed an increase in ROS fluorescence stimulated by LPS and hypoxia, indicating that an increased level of ROS production was highly correlated with inflammation severity. Compared with Z@P MNs, the cells exhibited a 70.66 ± 0.65 % decrease in ROS fluorescence intensity after Z@P-M MNs treatment, which was attributed to the powerful ROS scavenging ability of MnO_2[54]. Z@P-M MNs further decreased the ROS fluorescence intensity by 30.81 ± 1.62 % under 5 min of 1 W/cm^2 808 nm NIR irradiation, indicating that active Z@P-M nanomotors could improve the ability to scavenge ROS (Fig. 5g, and Supplementary Fig. 23c). Subsequently, the anti-inflammatory effects of Z@P-M MNs were also evaluated by the gene expression levels of interleukin-1β (IL-1β), interleukin-6 (IL-6), and TNF-α (Fig. 5h). Z@P-M MNs significantly reduced the levels of IL-1β, IL-6 and TNF-α inflammatory factors, which were further decreased under 5 min of 1 W/cm^2 808 nm NIR irradiation. It indicated that the released Z@P-M nanomotors had superior motion and diffusion effects and exhibited efficient anti-inflammatory effects in the treatment of *C. acnes* infections.

Anti-acne ability and alleviation of ILC inhibition by Z@P-M MNs

Encouraged by the efficient antibacterial, anti-biofilm and anti-inflammation of Z@P-M MNs, acne models were established through intradermal *C. acnes* (2×10^9 CFU/mL) inoculation in dorsal tissue of female balb/c mice, subsequently randomized into 6 experimental cohorts (n = 5/group): acne, erythromycin, blank MNs, Z@P MNs, Z@P-M MNs, and NIR + Z@P-M MNs, where 1 W/cm^2 808 nm NIR irradiation was applied for 5 min. The female mice with different treatments were monitored with the changes of acne on day 0, 3, 5, and 7 (Fig. 6a). As shown in Fig. 6b, two days after the injection of *C. acnes* (day 0), acne-like protrusion was formed at the injection site, and the proliferation of *C. acnes* resulted in the localized infection, ulceration, and skin lesions. Erythromycin group effectively reduced the size of acne, but mild desquamation and skin dryness were still observed, which was attributed to the skin irritation caused by erythromycin ointment[55]. RhB labelled nanomotors were detected in skin tissues after pressing Z@P-M MNs patches on the acne surface and 5 min of 1 W/cm^2 808 nm NIR irradiation, indicating that the developed MNs could effectively penetrate the skin to release nanomotors, which was remained in the skin for at least 72 h. It was noteworthy that Z@P-M selectively accumulated in the hair follicles, which was the main colonization site of *C. acnes*, leading to excessive keratinization and microbial proliferation[56]. Therefore, Z@P-M can effectively target acne lesions (Supplementary Fig. 24).

After pressing the Z@P-M MNs patch on mouse skin for 5 min, followed by 5 min of 1 W/cm^2 808 nm NIR irradiation, IR photothermal images showed that the temperature rose to 45.22 °C during 5 min (Supplementary Fig. 25, 26). After treatment, the skin healing at the puncture site was assessed. As shown in Supplementary Fig. 27, after removing the patch, a noticeable pinhole appeared on the skin surface, which recovered within 30 min, with no obvious redness, swelling, and ulceration. H&E staining of the skin showed similar results, observing a distinct conical depression in the skin tissues, enhancing the skin delivery of Z@P-M. Moreover, hemolysis assay of Z@P-M (ZnO_2 concentration = 100 μg/mL) was also conducted. Under 5 min of 1 W/cm^2 808 nm NIR irradiation, the hemolysis rate of Z@P-M was 4.13 ± 0.49 % (Supplementary Fig. 28). H&E staining of the major organs including heart, liver, spleen, lungs, and kidneys (Supplementary Fig. 29) showed no evidence of organ damage. The above results demonstrated the favorable biosafety of Z@P-M MNs.

To further evaluate the effect of MNs on acnes, the female mice were euthanized on day 7, collection of bacterial and histological and immunohistochemical analysis of the skin at the acnes site were performed. On day 7, bacterial burden analysis showed that erythromycin group, Z@P MNs group, Z@P-M MNs group, and NIR + Z@P-M MNs group (5 min of 1 W/cm^2 808 nm NIR irradiation) exhibited a significant reduction in *C. acnes* colony counts compared with the acne group. Among these, NIR + Z@P-M MNs group (5 min of 1 W/cm^2 808 nm NIR irradiation) and erythromycin group exhibited comparable antibacterial efficacy, which was attributed to the synergistic effects of penetration and PTT effects provided by the Z@P-M (Supplementary Fig. 30). The level of inflammation in the skin was assessed by counting the number of inflammatory cells by H&E staining. In Fig. 6c and Supplementary Fig. 31, there was a large infiltration of inflammatory cells and follicle destruction in the skin tissues of the acne group and blank MNs group. For erythromycin, Z@P MNs, Z@P-M MNs, and NIR + Z@P-M MNs groups (5 min of 1 W/cm^2 808 nm NIR irradiation), the number of inflammatory cells was relatively reduced, but some extent of inflammatory infiltration was still present. The skin structures were more intact in the NIR + Z@P-M MNs group (5 min of 1 W/cm^2 808 nm NIR irradiation) compared with other groups. Moreover, the NIR + Z@P-M MNs group (5 min of 1 W/cm^2 808 nm NIR irradiation)

https://doi.org/10.1038/s41467-026-68376-6

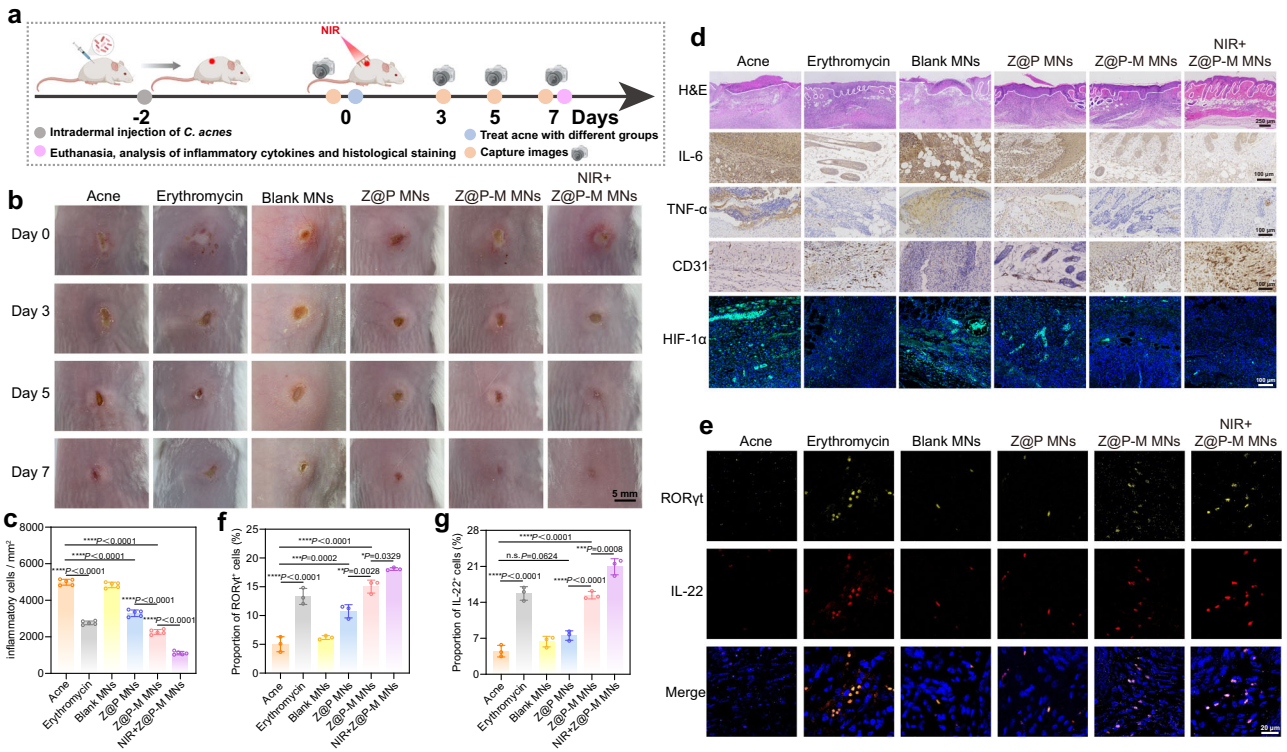

Fig. 6 | Anti-acne ability and alleviation of ILCs inhibition by Z@P-M MNs in vivo. a Schematic diagram of the in vivo experiment was created in BioRender by Hu, Z. (2025) https://BioRender.com/wd2r0cf. **b** Visual images of *C. acnes* infected acnes during different treatments, where 1 W/cm² 808 nm NIR irradiation was applied for 5 min (scale bar = 5 mm). $n = 5$ mice. **c** Inflammatory cells of the skins after different treatments, where 1 W/cm² 808 nm NIR irradiation was applied for 5 min. $n = 5$ mice. **d** Staining of skin tissue sections including H&E (scale bar = 250 μm), IL-6 (scale bar = 100 μm), TNF-α (scale bar = 100 μm), CD31 (scale bar = 100 μm), and HIF-1α (scale bar = 100 μm) after treating with (1) *C. acnes*, (2) erythromycin, (3) blank MNs, (4) Z@P MNs, (5) Z@P-M MNs, (6) NIR + Z@P-M MNs, where 1 W/cm² 808 nm NIR irradiation was applied for 5 min. The green and blue fluorescence represented HIF-1α and cell nucleus, respectively. $n = 5$ mice. **e** Immunofluorescence of RORγt and IL-22 in skin tissues after different treatments, where 1 W/cm² 808 nm NIR irradiation was applied for 5 min. The yellow, red, and blue fluorescence represented RORγt, IL-22, and cell nucleus, respectively (scale bar = 20 μm). $n = 3$ mice. Proportion of RORγt⁺ (**f**) and IL-22⁺ (**g**) cells after different treatments, where 1 W/cm² 808 nm NIR irradiation was applied for 5 min. $n = 3$ mice. Data in (**c**), (**f**), and (**g**) were presented as Mean ± SD and *P* values were analyzed by one-way ANOVA with Tukey's multiple comparisons test (n.s. represented no significance, $^{*}P < 0.05$, $^{**}P < 0.01$, $^{***}P < 0.001$, $^{****}P < 0.0001$). Source data are provided as a Source Data file.

showed normalized hair follicle structure and had the highest number of hair follicles. Histological analysis revealed significant inflammatory cells reduction in NIR + Z@P-M MNs group (5 min of 1 W/cm² 808 nm NIR irradiation), correlating with favorable therapeutic outcomes (Fig. 6d). Then we further analyzed IL-6 and TNF-α by immunohistochemistry. Anaerobic *C. acnes* overproliferated in sebaceous gland cells of mouse skin to form biofilms, which further caused hypoxia, promoted bacterial proliferation, led to inflammation, and upregulated the expression of IL-6 and TNF-α, both of the proteins were expressed at acne[4,57,58]. Optical density analysis showed that the expression levels of IL-6 and TNF-α were reduced by 37.03 ± 1.30 % and 54.66 ± 4.09 % in the Z@P-M MNs group compared to the Z@P MNs group. The expression of IL-6 and TNF-α in Z@P-M MNs was the lowest after NIR light treatment (Fig. 6d, and Supplementary Fig. 33a-b). As reported, the anti-inflammatory factor interleukin 10 (IL-10) could inhibit the production of pro-inflammatory cytokines, thereby reducing the inflammation[59]. The expression level of IL-10 in the Z@P-M MNs group was increased by 31.92 ± 5.08 % compared with that in the Z@P MNs group, and the level of IL-10 was further increased after 5 min of 1 W/cm² 808 nm NIR irradiation (Supplementary Fig. 32, and Supplementary Fig. 33c). These findings suggested that NIR + Z@P-M MNs treatment effectively activated the expression of anti-inflammatory genes, thereby downregulating pro-inflammatory factors and alleviating tissue inflammation.

Although it has been demonstrated that Z@P-M MNs could efficiently eliminate *C. acnes* and inflammation in vivo, their effects on the skin microbiome were not negligible. *C. acnes* and *Staphylococcus epidermidis* are commensal bacteria of the skin, exhibiting a relationship of mutual inhibition[7,60]. Inflammation and microbial imbalance caused by the over-proliferation of *C. acnes* can lead to acne[61]. Regarding the above issues, the sustained oxygen release of Z@P-M MNs alleviated the anaerobic environment in acne lesions, thereby inhibiting *C. acnes* proliferation. Most skin microbiota, including *Staphylococcus epidermidis*, were aerobic bacteria, oxygen generation contributed to restoring abundance of them, thereby further inhibiting the proliferation of *C. acnes* and re-establishing the microbial homeostasis of skin[62]. Z@P-M exhibited follicle-targeting properties, enabling more precise and safer elimination of *C. acnes* to promote the restoration of skin microbiota homeostasis. In future clinical applications, monitoring the skin microbiome through techniques such as 16S rRNA sequencing, metagenomic sequencing, and spatial omics will advance our understanding of the relationship between microneedling and skin microbiome[63]. The hypoxia level of MNs-treated tissues was also explored. HIF-1α, a classical marker of tissue hypoxia[64], was expressed at a lowest level in the NIR + Z@P-M MNs group (5 min of 1 W/cm² 808 nm NIR irradiation) compared with the other groups (Fig. 6d, and Supplementary Fig. 33d). It was attributed to the large amount of H_2O_2 released from ZnO_2 being converted into adequate oxygen supply by MnO_2, which attenuated the acne inflammation. In addition, the favorable propulsion and PTT effect of NIR light-actuated Z@P-M nanomotors could efficiently clear *C. acnes* biofilm, thus further reducing the inflammation level of acnes. Acnes caused by *C.*

acnes infection often ruptured leading to wound infection, resulting in severe scarring[65]. Angiogenesis played an essential role in wound healing, and CD31 was an important marker for neovascularization[66]. In Fig. 6d and Supplementary Fig. 33e, The expression level of CD31 in the Z@P MNs group was increased by 35.92 ± 4.99 % compared with that in the blank MNs group, owing to the fact that Zn^{2+} produced by the decomposition of ZnO_2 could promote tissue healing[55]. expression level of CD31 in the Z@P-M MNs group was increased by 32.08 ± 3.59 % compared with that in the Z@P MNs group, and the expression level of CD31 in the Z@P-M MNs group was further enhanced by 46.01 ± 3.87 % after 5 min of 1 W/cm^2 808 nm NIR irradiation, suggesting that 808 nm NIR irradiation accelerated the release of O_2 from Z@P-M MNs to alleviate the hypoxic microenvironment of acnes, thus promoting the healing of acne ulcer wounds.

ILCs are considered as one of the potential immune targets for microbial host interactions in acne. Previous studies have shown that bEVs of *C. acnes* can significantly reduce the number of ILCs, especially RORγt$^+$ ILCs[8]. Therefore, exploring the effect of Z@P-M MNs on the restoration of ILCs homeostasis in *C. acnes*-infected acnes may be an important target for acne treatment. We carried out the immunofluorescence staining of acne skin for IL-22 and RORγt (Fig. 6e). The cells releasing IL-22 and expressing RORγt were identified as ILC3[67]. Immunofluorescence results showed that IL-22 and ILC3 were almost not expressed in the acne and blank MNs groups, whereas the cells co-localized with IL-22 and RORγt were observed in the NIR + Z@P-M MNs group. It indicated that ILC3 was significantly inhibited in the acne and blank MNs groups, while the NIR + Z@P-M MNs group (5 min of 1 W/cm^2 808 nm NIR irradiation) could restore the homeostasis of ILC3 (Fig. 6f). It was attributed that enhanced diffusion of Z@P-M nanomotor synergized with PTT effect to further eliminate the over-accumulation of *C. acnes* and ultimately restored the ILC3 homeostasis. Moreover, IL-22 released from ILC3 was also significantly increased in the NIR + Z@P-M MNs group (Fig. 6g). Since IL-22 is a key cytokine for anti-infection and tissue reparation[68], it made sense that acne lesions were ideally healed in the NIR + Z@P-M MNs group.

Discussion

In our study, we successfully fabricate a NIR light-driven nanomotors loaded MN system for enhanced *C. acnes* biofilm penetration, which significantly facilitates acne treatment. Z@P-M nanomotors are prepared by asymmetric modification of in situ grown MnO_2/PDA layer on ZnO_2 through interfacial energy regulation. Then Z@P-M MNs are successfully fabricated by mixing Z@P-M nanomotors with sodium hyaluronate. The resulting MNs patch release active Z@P-M nanomotors in acne tissues through transdermal delivery. In the acidic biofilm microenvironment, Z@P-M nanomotors slowly release H_2O_2 to generate sufficient O_2 supply catalyzed by MnO_2, which alleviates the hypoxia of the biofilm microenvironment, eliminated inflammation, and ultimately promotes the healing of infected tissues. The asymmetric structure of the Z@P-M nanomotor generates self-thermophoresis actuated by NIR light. It further increases the diffusion of the nanomotor to achieve deep biofilm penetration synergizing with PTT effect to eradicate the *C. acnes* biofilm, thereby restoring the ILCs homeostasis in the infected tissues. In summary, the developed MN system provides a potential platform for acne treatment and regulatory application of MN system by in situ self-supplying of O_2 synergizing with PTT. However, most studies on MNs still remain in preclinical exploration, lacking sufficient clinical data and unpredictable obstacles to clinical translation[69]. Although our Z@P-M MNs patch contains biocompatible sodium hyaluronate approved by US Food and Drug Administration[70], it is still necessary to evaluate the potential allergenicity and irritation of Z@P-M in clinic. The degradation and clearance of Z@P-M in vivo should also be monitored and evaluated through long-term toxicity evaluation.

Method

Cell lines and animals

Mouse embryonic fibroblast cells (NIH3T3 cells, CL-0171) and mouse monocytic macrophage leukemia cells (RAW 264.7 cells, CL-0190) were obtained from Procell. Human keratinocytes cells (HaCaT cells, AW-CH0096) were purchased from AnWei-Sci. NIH3T3 cells, RAW 264.7 cells, and HaCaT cells were cultured in high glucose Dulbecco's Modified Eagle Medium (DMEM) supplemented with 10 % FBS and 1 % penicillin-streptomycin. The animal experiments were approved by the Institutional Animal Care and Use Committee (IACUC) of Southern Medical University (License No. SMUL202311048). Female balb/c mice (6 weeks old, 25 - 30 g) were purchased from the Laboratory Animal Center of Southern Medical University. These female balb/c mice were allowed free access to food and water and were fed under conditions of ambient temperature (21 − 26 °C), humidity (50 − 60 %), and a 12 h dark/light cycle.

Material

Polyvinylpyrrolidone (PVP Mw ≈ 58,000), isopropanol (IPA, ≥ 99 %), ammonia solution (28 %), dopamine hydrochloride (DA, ≥ 99 %), crystal violet (CV, ≥ 98 %), and Rhodamine B (RhB, ≥ 98 %) were purchased from Innochem (China). Polyacrylic acid (PAA) was obtained from Sigma Aldrich. H_2O_2 (30 %) was bought from Guangzhou Chemical Reagent Factory (China). Fluid thioglycollate medium was bought from Huankai Microbial (China). $[Ru(dpp)_3]Cl_2$ was obtained from Maokang Biotechnology (China). Zinc chloride ($ZnCl_2$, ≥ 99.99 %) and sodium hyaluronate was bought from Macklin (China). Cell counting kit-8 (CCK-8), Calcein-AM/PI, H_2O_2 detection assay kit, ROS detection assay kit, 4′,6-diamidino-2-phenylindole (DAPI), and Hoechst 33342 were obtained from Biyotime (China). 5-carboxyfluorescein diacetate (5-CFDA, ≥ 98 %) was obtained from YuanyeBio-Technology (China). One-step TUNEL In Situ Apoptosis Kit was obtained from Elabscience (China). Hematoxylin-Eosin (H&E) Stain Kit were purchased from Solarbio Life Sciences (China). Primers of IL-1β, IL-6 and TNF-α were obtained from Sangon Biotech (China). Total RNA isolation kit was bought from Foregene (China). Rever Tra Ace qPCR RT kit and SYBR Green Master were obtained from Yeasen (China). HIF-1α monoclonal antibody was obtained from Cell Signaling Technology (America). IL-6 polyclonal antibody, TNF-α polyclonal antibody, CD31 polyclonal antibody and IL-10 recombinant antibody were bought from Proteintech (China). APC-RORγt monoclonal antibody was obtained from Invitrogen (America). PE-anti-mouse IL-22 antibody was obtained from Biolegend (America). Chromogen was bought from ZSGB-BIO (China). AnaeroPack and anaerobic culture box (2.5 L) were obtained from Mitsubishi (Japan).

Instruments

The structure of NPs and bacterial samples was observed using a JEM 1400 TEM under 120 kV acceleration voltage (JEOL, Japan). Elemental analyses of Z@P-M were measured by Oxford X-MaxN 80 T IE250, UK. Elemental composition of Z@P-M MNs was conducted via EDS (Phenom ProX, 15 kV, Netherlands). The structure of Z@P-M MNs and bacterial samples were observed by scanning electron microscope (SEM) (Phenom, Netherlands). Mechanical properties of MNs were measured by electronic universal testing machine (SANS, China). The size and zeta potential were characterized by Zetasizer Nano ZSE (Malvern, UK). XPS spectra was performed by X-ray photoelectron spectroscopy (Thermo SCIENTIFIC ESCALAB 250Xi, America) and analyzed by Avantage software (version 5.9931). FTIR spectra were measured by FTIR spectrometer (Nicolet 380, Thermo). The crystalline profile was measured by X-ray diffractometer (Bruker D2, Germany). Raman spectra were measured by laser confocal microscope raman spectrometer (RENISHAW inVia, UK). The release rate of Zn^{2+} was quantified by Inductively coupled plasma mass spectrometry (ICP-MS) (Agilent, America). Samples of Zn^{2+} detection were digested by

microwave digestion system (Preekem, China). Thermal images were captured by infrared thermography (Fluke, America). Heating curves were obtained by infrared thermography (YOSEEN INFRARED, China). UV-Vis-NIR spectra were acquired using UV-2600 spectrophotometer (SHIMADZU, Japan). Absorbance of UV-Vis was measured by multifunctional microplate inspection system (Tecan, Switzerland). The release level of oxygen was quantified by dissolved oxygen analyzer (LEICI, China). Fluorescence images of ROS, HIF-1α, and $[Ru(dpp)_3]Cl_2$ in vitro and the motion of Z@P-M nanomotors were captured by an inverted microscope (Nikon, Japan). Three-dimensional porcine skin was reconstructed through z-stack imaging via CLSM (Nikon, Japan). Three-dimensional biofilms was reconstructed through z-stack imaging via CLSM (Zeiss, Germany). H&E and immunohistochemical slides were scanned by Slide Scan System SQS-1000 (Teksqray, China).

Synthesis of Z

$ZnCl_2$ (135 mg) and PVP (690 mg) were completely dissolved in 30 mL anhydrous ethanol, then 2 mL ammonia (10 M) was added. When the solution turned clear, 2 mL of 30 % H_2O_2 was slowly dropped under stirring, and the reaction lasted for 1 day. The collected ZnO_2 was wash 3 times by ethanol and stored in anhydrous ethanol.

Synthesis of Z@P-M nanomotors

Z@P-M were synthesized based on the modified method[21,71]. Briefly, 10 mg ZnO_2, 1 mL ammonia (2 M), and 7.5 mg PAA were dispersed in 15 mL ultrapure water. Subsequently, 96 mL IPA was slowly dropped uder stirring. After 1 h, 2 mL ammonia (10 M) and 1 mg DA were added in turn and the reaction was conducted for 4 h at 50 °C. Z@P was then collected and washed 3 times with ethanol. 1 mg Z@P and 500 μL $KMnO_4$ (2 mg/mL) were dispersed in ultrapure water (10 mL), stirring for 20 min. After ultrapure water and ethanol washing, Z@P-M was collected and stored in ethyl alcohol. As control group, Z#P-M was ZnO_2 fully coated by PDA and MnO_2. The synthesis of Z#P-M was carried out in ultrapure water without IPA, and the remaining steps were consistent with above.

Preparation of MNs patches

For Z@P-M MNs patch, 150 mg sodium hyaluronate was dissolved in 1 mL ultrapure water containing Z@P-M (ZnO_2 concentration = 100 μg/mL), then the solution was dropped in MN mold. After 15 min vacuum drying, the mold was dried at 40 °C for 5 h. Blank MNs patch shared the same fabrication process without adding Z@P-M.

Degradation of Z@P-M MNs

Z@P-M MNs was incubated in 70 % humidity box at 25 °C for 30 min. Bright-field morphologic images were captured at 0, 10, 20, 30 min, respectively.

Detection of Zn^{2+} level

ICP-MS was used to detect Zn^{2+} level. Z@P-M NPs (ZnO_2 concentration = 100 μg/mL) were incubated in 5 mL buffer at pH 5.5 and 7.4 during 24 h. The centrifuged supernatant samples (100 μL) at different time points (2 h, 4 h, 8 h, 12 h, and 24 h) were collected and treated by 10 mL 10 % nitric acid (HNO_3). The samples were digested by microwave digestion system, with the temperature increasing to 180 °C during 30 min, and maintained at that temperature for 60 min. Finally, the samples were diluted to a solution containing 3 % HNO_3, filtered through a 0.22 μm filter, and Zn^{2+} concentration was measured by ICP-MS.

Release of H_2O_2

1 mL of Z, Z@P, and Z@P-M NPs (ZnO_2 concentration = 1 mg/mL) were dispersed in 9 mL buffer (pH 5.5 or 7.4) at 37 °C. H_2O_2 release levels at different time points was measured using a hydrogen peroxide assay kit. H_2O_2 levels were detected by mixing the samples with dimethylphenol orange, incubating for 20 min at 37 °C, finally measuring absorbance at 560 nm. Standard curve was $A_{560nm} = 0.0014C_{H2O2} + 0.0733$ (Supplementary Fig. 34).

O_2 release

1 mL of Z, Z@P, and Z@P-M NPs (ZnO_2 concentration = 1 mg/mL) were dispersed in 9 mL buffer (pH 5.5 or 7.4) at 37 °C, with deoxygenation in a nitrogen atmosphere. Oxygen generation was monitored by dissolved oxygen analyzer during 6 h and the data were recorded per 10 s.

Photothermal properties

Temperature curves of Z@P-M NPs (ZnO_2 concentration = 0 − 200 μg/mL) were evaluated under 808 nm irradiation (1 W/cm^2, 10 min). Z@P-M samples (ZnO_2 concentration = 100 μg/mL) was exposed to 808 nm NIR light (0.5, 1, and 1.5 W/cm^2, 10 min) and the temperature curves were recorded. Z, Z@P, and Z@P-M solution with the same ZnO_2 concentration (100 μg/mL) was collected in a 1.5 mL EP tube with PBS as control. All samples were exposed to 808 nm NIR radiation at 1 W/cm^2 for 10 min and the IR photothermal images and temperature curves were recorded. 8 heating/cooling cycles of Z@P-M (ZnO_2 concentration = 100 μg/mL) and Z@P-M MNs were performed with 1 W/cm^2 808 nm NIR irradiation to investigate the photothermal stability. Z@P-M MNs and blank MNs were treated with 808 nm NIR irradiation (1 W/cm^2, 5 min), the temperature curves and IR photothermal images were recorded.

Photothermal conversion efficiency

Z@P-M NPs (ZnO_2 concentration = 100 μg/mL) were treated with 1 W/cm^2 808 nm NIR irradiation for 600 s. And the temperature curve and conversion efficiency (η) were analyzed. The η was derived from Eq. (1):

$$\eta = \frac{hS(T_{\max} - T_{surr}) - Q_{dis}}{I(1 - 10^{-A_{808}})} \tag{1}$$

h was heat-transfer-coefficient, S represented the surface area of the container, T_{max} indicated the equilibrium temperature, T_{surr} signified the ambient temperature of the surroundings, Q_{dis} represented the heat associated with the light absorbance by the solvent, I was the 808 nm NIR light power (1 W/cm^2), and A_{808} represented the absorbance of Z@P-M NPs at 808 nm (Supplementary Fig. 35). hS was derived from Eq. (2):

$$\tau_s = \frac{m_D C_D}{hS} \tag{2}$$

m_D and C_D were the weight (0.5 g) and heat capacity (4.2 J/g) of pure water, was calculated from Eq. (3):

$$t = \tau_s \ln\left(\frac{T_{RT} - T_{surr}}{T_{Max} - T_{surr}}\right) \tag{3}$$

T_{RT} was calculated from time-temperature curves during 900 s passive cooling phase.

Evaluation of skin penetration of Z@P-M MNs

Fresh porcine skin was purchased from the supermarket, placed in a clean Petri dish with the stratum corneum facing upward, and kept moist. Z@P-M MNs (loaded with RhB labelled Z@P-M) were inserted into the porcine skin for 5 min, followed by 1 W/cm^2 808 nm NIR irradiation for 5 min. Finally, the treated porcine skin (insert 5 min, 1 W/cm^2 808 nm NIR light irradiated for 3 min or 5 min) was z-stack scanned by CLSM.

Antibiofilm assay

The used bacterial strains were *MRSA* (ATCC 43300) and *C. acnes* (ATCC 6919). *MRSA* and *C. acnes* were proliferated in Luria-Bertani (LB) medium and thioglycollate medium to mid-log phase, respectively. 1 mL of bacterial suspension (1×10^8 CFU/mL) was seeded in 24-well plates. *C. acnes* were incubated under hypoxic conditions and *MRSA* was cultivated under aerobic conditions. Biofilms were formed through 48 h incubation with medium replenishment at 24 h interval, followed by gentle PBS washing to remove planktonic bacteria. The culture medium was removed, and the formed biofilms were gently washed twice with PBS. Different treatments were performed on the biofilms, including (1) control, (2) blank MNs, (3) Z@P MNs, (4) Z@P-M MNs, (5) NIR + Z@P-M MNs, where 1 W/cm^2 808 nm NIR irradiation was applied for 5 min. The control group was treated with PBS. After 5 min co-culture, NIR + Z@P-M MNs group was treated with 1 W/cm^2 808 nm NIR irradiation for 5 min. To evaluate the antibiofilm effects of different duration of 808 nm NIR irradiation, the samples were divided into 4 groups: (1) control, (2) Z@P-M MNs, (3) 3 min NIR + Z@P-M MNs, and (4) 5 min NIR + Z@P-M MNs, where 1 W/cm^2 808 nm NIR irradiation was applied. The following procedures were consistent with those described above. After 6 h co-incubation, CV staining was performed on biofilms. The resulting biofilms were washed twice with PBS, then stained with 0.1 % CV for 10 min. After gently washing, the biofilms were photographed and dissolved with 500 μL of anhydrous ethanol. The biomass of the biofilms was then quantified by recording the absorbance at 595 nm.

Biofilm morphology

Biofilms were fixed with 4 % paraformaldehyde at 4 °C for 2 h. Washing with PBS three times, biofilms were dehydrated with gradient ethanol (20 %, 40 %, 60 %, 80 %, and 100 %) and tert-butyl alcohol for 15 min, respectively. Finally, the dehydrated samples were freeze-dried and sprayed with a gold layer for SEM observation.

Penetration of Z@P-M in biofilms

The culture medium of the mature biofilms was removed, and the formed biofilms were gently washed twice with PBS. RhB-labelled Z#P-M and Z@P-M NPs (ZnO_2 concentration = 100 μg/mL) were gently added to the biofilms and incubated for 20 min. Group NIR + Z#P-M and group NIR + Z@P-M were irradiated with 1 W/cm^2 808 nm NIR light for 5 min, followed by gently removing the supernatant. Subsequently, the biofilms were stained with 5-CFDA and carefully washed twice with PBS. Finally, Z-stack scanning was performed by CLSM (green represents biofilm, and red represents NPs).

Standard plate counting assay

Antimicrobial rates of all samples were analyzed by standard plate counting assays. 1 mL of *C. acnes* suspension (2×10^5 CFU/mL) was added to sterile 5 mL EP tube and different treatments were performed, including (1) control, (2) blank MNs, (3) Z@P MNs, (4) Z@P-M MNs, (5) NIR + Z@P-M MNs, where 1 W/cm^2 808 nm NIR irradiation was applied for 5 min. The control group was treated with PBS. Samples were incubated for 6 h. After the treatment, 200 μL of 100-fold diluted bacterial solution was collected, spread on thioglycollate agar plates and incubated anaerobically at 37 °C for 2 days. Similarly, after *MRSA* was subjected to the above treatment, the diluted bacterial solution was spread on Luria-Bertani agar plates and incubated aerobically at 37 °C for 1 day. Microbial viability was calculated as: Survival rate (%) = ($CFU_{experimental\ groups}$ / $CFU_{control\ group}$) × 100. To evaluate the antibiofilm effects of different duration of 808 nm NIR irradiation, the samples were divided into 4 groups: (1) control, (2) Z@P-M MNs, (3) 3 min NIR + Z@P-M MNs, and (4) 5 min NIR + Z@P-M MNs, where 1 W/cm^2 808 nm NIR irradiation was applied. Other procedures were consistent with those described above.

TUNEL staining

The treated biofilms were fixed with 4 % paraformaldehyde for 10 min and washed 3 times with PBS. TUNEL fluorescence was detected by the One-step TUNEL In Situ Apoptosis Kit.

Cell viability

For cytotoxicity assays, 5×10^3 NIH3T3 cells/well in 96-well plates were exposed to Z@P-M (ZnO_2 concentration = 0 − 200 μg/mL) for 12 h via CCK-8 method, absorbance at 450 nm was measured by microplate reader (Biotek800 TS). 6×10^5 NIH3T3 cells/well, 6×10^5 RAW 264.7 cells/well, and 6×10^5 HaCaT cells/well were seeded in 24-well plates, treated with different groups, where 1 W/cm^2 808 nm NIR irradiation was applied for 5 min. Washing with PBS and staining with Calcein AM/PI for 15 min, the cells were captured under inverted fluorescence microscope and the number of live and dead cells was calculated by Image J.

Cellular uptake

3×10^5 NIH3T3 cells/well were seeded in 24-well plates and treated with different groups. Cellular uptake of RhB labelled Z@P-M MNs and Z#P-M MNs were assessed following 6 h co-incubation with NIH3T3 cells and subsequent 5 min of 1 W/cm^2 808 nm NIR irradiation. Cytoskeleton was labelled with Actin-Tracker Green-488, which was diluted 1:100 and incubated with cells for 1 h. Finally, the fluorescence images were captured by CLSM.

Migration capability of NIH3T3 cells

NIH3T3 cells were digested and planted on 6-well plates (3×10^6 NIH3T3 cells/well). Using a 200 μL pipette tip, scrape the monolayer of cells when confluence reaches 90 %. Then cells were cultured in hypoxia. The cell pictures were captured by inverted fluorescence microscope and the wound area and healing rates were calculated at different time point (0 h, 18 h and 36 h).

$$\text{Migration}\% = (\text{Scratcharea}_{0h} - \text{Scratcharea}_{18hor36h})/\text{Scratcharea}_{0h} \times 100. \quad (4)$$

Intracellular O_2 detection

Intracellular oxygen levels were quantified using $[Ru(dpp)_3]Cl_2$ oxygen-sensitive nanoprobes. The fluorescence of the probe can be strongly extinguished by O_2. 3×10^5 NIH3T3 cells/well were seeded in 24-well plates and cultured for 24 h, the cells were treated with PBS, blank MNs, Z@P MNs, Z@P-M MNs, and NIR + Z@P-M MNs for 6 h under hypoxia, where 1 W/cm^2 808 nm NIR irradiation was applied for 5 min. Then cells were incubated with the oxygen sensing probe for 4 h. Cells cultured under normoxia as control. The fluorescence intensity was recorded by inverted fluorescence microscope.

Intracellular ROS detection

3×10^5 NIH3T3 cells/well were seeded in 24-well plates and cultured for 24 h. Then cells were treated with PBS, blank MNs, Z@P MNs, Z@P-M MNs, and NIR + Z@P-M MNs under hypoxic condition in medium containing LPS (1 μg/mL) for 12 h, where 1 W/cm^2 808 nm NIR irradiation was applied for 5 min. Cells cultured under normoxia as control. The cells were then incubated with DCFH-DA (10 μM) for 2 h, while Hoechst 33342 was used to labelled the nuclei. Finally, the fluorescence figures were captured by inverted fluorescence microscope.

Immunofluorescence in vitro

3×10^5 NIH3T3 cells/well were seeded in 24-well plates and cultured for 24 h. Cells were treated with PBS, blank MNs, Z@P MNs, Z@P-M MNs, and NIR + Z@P-M MNs under hypoxic condition in medium containing

LPS (1 μg/mL) for 12 h, where 1 W/cm² 808 nm NIR irradiation was applied for 5 min. Cells cultured under normoxia as control. HIF-1α primary antibody and RhB labelled secondary antibody were used to stain the cells. F-actin was stained by Actin-Tracker Green-488.

qRT-PCR

3×10^6 NIH3T3 cells/well were plated in 6-well plates and cultured for 24 h. Cells were treated with PBS, blank MNs, Z@P MNs, Z@P-M MNs, and NIR + Z@P-M MNs under hypoxic condition in medium containing LPS (1 μg/mL) for 12 h, where 1 W/cm² 808 nm NIR irradiation was applied for 5 min. Cells cultured under normoxia as control. Total RNA isolation of NIH3T3 cells were extracted by super total RNA extraction kit and reverse transcribed to cDNA using cDNA ReverTra Ace qPCR RT kit. PCR was conducted at 95 °C, 10 min denaturation, 57 °C, 10 s annealing, 60 °C, and 10 s extension. The PCR reaction system is 5 μL of 2×SYBR Green Master, primer (0.3 μL) and cDNA (1 μL) and RNase Free dH_2O (3.4 μL). The relative expression was calculated using the $2^{\triangle\triangle Ct}$ method. Normalization was based on GAPDH expression levels. Supplementary Table 1 showed the primer sequences.

Acne model establishment and treatment

After female balb/c mice were anaesthetized, the hair on the backs of the female mice was exfoliated with a shaver and depilatory cream, and sterilized with 75 % ethanol. To establish an acne vulgaris model, 100 μL of *C. acnes* inoculum (2×10^9 CFU/mL) was administered via intradermal inoculation along the dorsal region on day -2. Experimental cohorts consisting of 5 female mice per group were randomly allocated into 6 groups: acne, erythromycin, blank MNs, Z@P MNs, Z@P-M MNs, and NIR + Z@P-M MNs, where 1 W/cm² 808 nm NIR irradiation was applied for 5 min. On day 0, the acne group and erythromycin group were treated with PBS solution and erythromycin ointment, respectively. The blank MNs group, Z@P MNs group, and Z@P-M MNs group were treated by pressing the MNs patches onto the dorsal skin for 5 min before removal. For NIR + Z@P-M MNs group, Z@P-M MNs patches were pressed onto the dorsal skin of female mice for 5 min, followed by irradiation with 808 nm NIR light (1 W/cm²) for 5 min, and finally the patches were removed. the dorsal skin of female mice was photographed on day 0, 3, 5, and 7. On day 7, the collected bacterial samples from the female mice wounds were spread on thioglycollate agar plates to observe bacterial burden. After the female mice were euthanized, the skin was cut 5 mm along the wound edge to acquire skin tissues. The collected skin tissues, heart, liver, spleen, lung, and kidney tissues were fixed, permeabilized, embedded in paraffin, and sectioned.

The biocompatibility of Z@P-M MNs in vivo

Z@P-M MNs were pressed onto the dorsal skin of the female mice for 5 min, followed by 1 W/cm² 808 nm NIR light irradiation for 5 min. After the treatment, the patches were gently removed, and the images of the dorsal skin and H&E staining of skin tissues at different time points (0 − 30 min) were collected. Optical images of the MNs patches before and after application were also captured.

H&E staining

Histological specimens underwent sequential processing commencing with xylene-mediated deparaffinization, followed by ethanol gradient rehydration. Staining protocols initiated with hematoxylin counterstaining (5 min), succeeded by aqueous differentiation (deionized H_2O, 3 min) and acidic differentiation (1 % HCl/ethanol, 30 s), culminating in eosin counterstaining (0.5 % w/v, pH 5.5) for cytoplasmic visualization. The images were obtained using a Slide Scan System SQS-1000.

Hemolysis assay

Fresh mouse blood was centrifuged at 4 °C at 860 g for 15 min to obtain a red blood cell pellet. The red blood cells were washed 3 times with PBS and diluted to a final concentration of 5 % (v/v). Different treatments were applied to 1 mL of the red blood cell suspension, including: (1) dd H_2O, (2) PBS, (3) Z@P-M, (4) NIR + Z@P-M, where 1 W/cm² 808 nm NIR irradiation was applied for 5 min, followed by incubation at 37 °C for 4 h. After treatment, the samples were centrifuged at 860 g at 4 °C for 10 min to collect the supernatant, and the optical density (OD) value was measured at 570 nm. The hemolysis rate was calculated using the following formula.

$$\text{Hemolysis}\% = [(OD_{sample} - OD_{negative})/(OD_{positive} - OD_{negative})] \times 100. \quad (5)$$

IHC

Paraffin-embedded tissue sections underwent antigen retrieval followed by incubation with IL-6, TNF-α, CD31, and IL-10 primary antibodies (4 °C, 16 h) and secondary antibodies (25 °C, 1 h). After staining with chromogen, the images were obtained using a Slide Scan System SQS-1000.

Immunofluorescence in vivo

Histological preparations underwent standard dewaxing in xylene followed by ethanol gradient hydration. Antigen retrieval was performed by sodium citrate buffer (pH 6.0). Subsequently, samples were incubated with 0.5 % Triton X-100 for 15 min, blocking with 5 % BSA (25 °C, 60 min), and primary antibody incubation targeting HIF-1α (1:1000 dilution, 4 °C, 16 h). Following triple PBS washes, the samples were incubated with fluorescent secondary antibodies for 1 h and labelled with DAPI. RORγt and IL-22 detection was incubated 1:100 with RORγt and IL-22 primary antibodies overnight. The images were captured by CLSM.

Statistical analysis

Each experiment was conducted three times or more. The experimental data were presented as mean ± SD. Statistical analysis were used by one-way ANOVA with Tukey's multiple comparisons test (n.s. represented no significance, $^*P < 0.05$, $^{**}P < 0.01$, $^{***}P < 0.001$, $^{****}P < 0.0001$). $P < 0.05$ was statistically significant.

Reporting summary

Further information on research design is available in the Nature Portfolio Reporting Summary linked to this article.

Data availability

Source data are provided with this paper. The source data produced by this study can be found in the Supplementary Information/Source Data file. The source data are available in Figshare dataset: https://doi.org/10.6084/m9.figshare.30226972. All data supporting the findings of this study are available from corresponding authors upon request. Source data are provided with this paper.

References

1. Williams, H. C., Dellavalle, R. P. & Garner, S. Acne vulgaris. *Lancet* **379**, 361–372 (2012).
2. Layton, A. M. & Ravenscroft, J. Adolescent acne vulgaris: current and emerging treatments. *Lancet Child Adolesc. Health* **7**, 136–144 (2023).
3. Brüggemann, H. et al. The complete genome sequence of Propionibacterium acnes, a commensal of human skin. *Science* **305**, 671–673 (2004).
4. Xiang, Y. et al. Ultrasound-triggered interfacial engineering-based microneedle for bacterial infection acne treatment. *Sci. Adv.* **9**, eadf0854 (2023).
5. Zhang, T. et al. Active pharmaceutical ingredient poly(ionic liquid)-based microneedles for the treatment of skin acne infection. *Acta Biomater.* **115**, 136–147 (2020).

6. Kobayashi, T. et al. Homeostatic control of sebaceous glands by innate lymphoid cells regulates commensal bacteria equilibrium. *Cell* **176**, 982–997.e916 (2019).
7. Gan, Y. et al. Commensal microbe regulation of skin cells in disease. *Cell Host Microbe* **32**, 1264–1279 (2024).
8. Xu, Y. et al. Innate lymphoid cell-based immunomodulatory hydrogel microspheres containing Cutibacterium acnes extracellular vesicles for the treatment of psoriasis. *Acta Biomater.* **184**, 296–312 (2024).
9. Reynolds, R.V. et al. Guidelines of care for the management of acne vulgaris. *J. Am. Acad. Dermatol.* **90**, 1006 (2024).
10. Wang, B. et al. Hyaluronic acid-based CuS nanoenzyme biodegradable microneedles for treating deep cutaneous fungal Infection without drug resistance. *Nano Lett.* **23**, 1327–1336 (2023).
11. Wu, C. et al. Microneedles as transdermal drug delivery system for enhancing skin disease treatment. *Acta Pharm. Sin. B* **14**, 5161–5180 (2024).
12. Zheng, B. et al. Microorganism microneedle micro-engine depth drug delivery. *Nat. Commun.* **15**, 8947 (2024).
13. Liu, Z. et al. Janus nanoparticles targeting extracellular polymeric substance achieve flexible elimination of drug-resistant biofilms. *Nat. Commun.* **14**, 5132 (2023).
14. Gao, J. et al. Hyperthermia-triggered biomimetic bubble nanomachines. *Nat. Commun.* **14**, 4867 (2023).
15. Yan, D. et al. Adding flying wings: butterfly-shaped NIR-II AIEgens with multiple molecular rotors for photothermal combating of bacterial biofilms. *J. Am. Chem. Soc.* **145**, 25705–25715 (2023).
16. Liu, T. et al. Controlled propulsion of micro/nanomotors: operational mechanisms, motion manipulation and potential biomedical applications. *Chem. Soc. Rev.* **51**, 10083–10119 (2022).
17. Xu, W. et al. Self-propelled ferroptosis nanoinducer for enhanced cancer therapy. *Int. J. Extrem. Manuf.* **7**, 035501 (2025).
18. Zhang, H. et al. A bioinspired virus-like mechano–bactericidal nanomotor for ocular multidrug-resistant bacterial infection treatment. *Adv. Mater.* **37**, 2408221 (2025).
19. Zhang, X. et al. Alginate lyase immobilized Chlamydomonas algae microrobots: minimally invasive therapy for biofilm penetration and eradication. *Acta Pharm. Sin. B* **15**, 3259–3272 (2025).
20. Ji, X. et al. multifunctional parachute-like nanomotors for enhanced skin penetration and synergistic antifungal therapy. *ACS Nano* **15**, 14218–14228 (2021).
21. Hu, Z. et al. NIR-actuated ferroptosis nanomotor for enhanced tumor penetration and therapy. *Adv. Mater.* **36**, 2412227 (2024).
22. Jia, D. et al. A self-supplied hydrogen peroxide and nitric oxide-generating nanoplatform enhances the efficacy of chemodynamic therapy for biofilm eradication. *J. Colloid Interface Sci.* **678**, 20–29 (2025).
23. Wang, J. et al. Carrier-free nanoprodrug for p53-mutated tumor therapy via concurrent delivery of zinc-manganese dual ions and ROS. *Bioact. Mater.* **20**, 404–417 (2023).
24. Li, L. et al. A MnO2 nanoparticle-dotted hydrogel promotes spinal cord repair via regulating reactive oxygen species microenvironment and synergizing with mesenchymal stem cells. *ACS Nano* **13**, 14283–14293 (2019).
25. Zhang, L. et al. Tailored synthesis of octopus-type janus nanoparticles for synergistic actively-targeted and chemo-photothermal therapy. *Angew. Chem.* **55**, 2118–2121 (2016).
26. Tiwari, N. et al. Nanocarriers for skin applications: where do we stand? *Angew. Chem.* **61**, e202107960 (2022).
27. Sabri, A. H. et al. Intradermal and transdermal drug delivery using microneedles – fabrication, performance evaluation and application to lymphatic delivery. *Adv. Drug Deliv. Rev.* **153**, 195–215 (2020).
28. Yu, W. et al. Polymer microneedles fabricated from alginate and hyaluronate for transdermal delivery of insulin. *Mater. Sci. Eng. C. Mater. Biol. Appl* **80**, 187–196 (2017).
29. Wang, J. et al. Oxygen vacancy induced band-gap narrowing and enhanced visible light photocatalytic activity of ZnO. *ACS Appl. Mater. Interfaces* **4**, 4024–4030 (2012).
30. Herring, N. P., Panchakarla, L. S. & El-Shall, M. S. P-type nitrogen-doped ZnO nanostructures with controlled shape and doping level by facile microwave synthesis. *Langmuir* **30**, 2230–2240 (2014).
31. Cheng, S. et al. Soft-template synthesis and characterization of ZnO2 and ZnO hollow spheres. *J. Phys. Chem. C.* **113**, 13630–13635 (2009).
32. Escobedo-Morales, A. et al. Structural and vibrational properties of hydrothermally grown ZnO_2 nanoparticles. *J. Cryst. Growth* **316**, 37–41 (2011).
33. Razzaq, H. A. A. et al. Bioactive films based on barley β-glucans and ZnO for wound healing applications. *Carbohydr. Polym.* **272**, 118442 (2021).
34. Salehi, N. et al. Synergistic photothermal and photodynamic therapy to promote bacteria-infected wound healing using ZnO@PDA/Ag-integrated waterborne polyurethane films. *J. Mater. Chem. B* **13**, 6177–6198 (2025).
35. Wang, Z. et al. A thrombin-activated peptide-templated nanozyme for remedying ischemic stroke via thrombolytic and neuroprotective actions. *Adv. Mater.* **36**, 2210144 (2024).
36. Ma, H. et al. Mesoporous Silica-based nanomotors loaded with rapamycin for synergistic treatment of rheumatoid arthritis. *ACS Nano* **19**, 22914–22930 (2025).
37. Du, Y. et al. Synergistic provoking of pyroptosis and STING pathway by multifunctional manganese-polydopamine nano-Immunomodulator for enhanced renal cell carcinoma immunotherapy. *Adv. Healthc. Mater.* **14**, 2500141 (2025).
38. Zeng, W. et al. Dual-response oxygen-generating MnO_2 nanoparticles with polydopamine modification for combined photothermal-photodynamic therapy. *Chem. Eng. J.* **389**, 124494 (2020).
39. Wang, C. et al. A self-regulated phototheranostic nanosystem with single wavelength-triggered energy switching and oxygen supply for multimodal synergistic therapy of bacterial biofilm infections. *Aggregate* **5**, e587 (2024).
40. Lai, S. et al. Fluorescent microneedle-based theranostic patch for naked-eye monitoring and on-demand photo-therapy of bacterial biofilm infections. *Adv. Funct. Mater.* **35**, 2415559 (2025).
41. Gao, S. et al. Chlorella-loaded antibacterial microneedles for microacupuncture oxygen therapy of diabetic bacterial infected wounds. *Adv. Mater.* **36**, 2307585 (2024).
42. Zhao, T. et al. Mesoporous nano-badminton with asymmetric mass distribution: how nanoscale architecture affects the blood flow dynamics. *J. Am. Chem. Soc.* **145**, 21454–21464 (2023).
43. Yang, Z.-R. et al. Endogenous stimuli-responsive separating microneedles to inhibit hypertrophic scar through remodeling the pathological microenvironment. *Nat. Commun.* **15**, 2038 (2024).
44. Achermann, Y., Goldstein Ellie, J. C., Coenye, T. & Shirtliff Mark, E. Propionibacterium acnes: from commensal to opportunistic biofilm-associated implant pathogen. *Clin. Microbiol. Rev.* **27**, 419–440 (2014).
45. Chen, Z., Wang, Z., Ren, J. & Qu, X. Enzyme mimicry for combating bacteria and biofilms. *Acc. Chem. Res* **51**, 789–799 (2018).
46. Xie, S. et al. Self-propelling nanomotors integrated with biofilm microenvironment-activated NO release to accelerate healing of bacteria-infected diabetic wounds. *Adv. Healthc. Mater.* **11**, 2201323 (2022).
47. Tyner, H. & Patel, R. Propionibacterium acnes biofilm – a sanctuary for Staphylococcus aureus? *Anaerobe* **40**, 63–67 (2016).

48. Wang, S. et al. Nanoenzyme-reinforced injectable hydrogel for healing diabetic wounds infected with multidrug resistant bacteria. *Nano Lett.* **20**, 5149–5158 (2020).
49. Wei, Y. et al. Kill two birds with one stone: dual-metal MOF-nanozyme-decorated hydrogels with ROS-scavenging, oxygen-generating, and antibacterial abilities for accelerating Infected diabetic wound healing. *Small* **20**, 2403679 (2024).
50. Zhang, X. et al. Wireless power supply near-infrared light drug-loaded microneedle system for the treatment of linear skin wounds. *Chem. Eng. J.* **500**, 157110 (2024).
51. Zhao, Y. et al. All-in-one bioactive properties of photothermal nanofibers for accelerating diabetic wound healing. *Biomaterials* **295**, 122029 (2023).
52. Ye, J. et al. Biomimetic dual-driven heterojunction nanomotors for targeted catalytic immunotherapy of glioblastoma. *Adv. Funct. Mater.* **35**, 2416265 (2024).
53. Yuan, Z. et al. A photo-therapeutic nanocomposite with bio-responsive oxygen self-supplying combats biofilm infections and inflammation from drug-resistant bacteria. *Adv. Funct. Mater.* **33**, 2302908 (2023).
54. Li, J. et al. Targeting endogenous hydrogen peroxide at bone defects promotes bone repair. *Adv. Funct. Mater.* **32**, 2111208 (2022).
55. Zhu, J. et al. Biomimetic hyaluronic acid-stabilized zinc oxide nanoparticles in acne treatment: A preclinical and clinical approach. *J. Control Release* **382**, 113754 (2025).
56. Jahns, A. C. & Alexeyev, O. A. Three dimensional distribution of Propionibacterium acnes biofilms in human skin. *Exp. Dermatol* **23**, 687–689 (2014).
57. Kim, Y., Lee, J. & Lee, J. Antibiofilm activities of fatty acids including myristoleic acid against Cutibacterium acnes via reduced cell hydrophobicity. *Phytomedicine* **91**, 153710 (2021).
58. Sharma, M., Schoop, R., Suter, A. & Hudson, J. B. The potential use of Echinacea in acne: control of Propionibacterium acnes growth and inflammation. *Phytother. Res* **25**, 517–521 (2011).
59. Lou, S. et al. Efficient organic nanoparticles for photothermal antibacterial activity and immune regulation to promote maxillofacial wound healing and scarless repair. *Biomaterials* **324**, 123534 (2026).
60. Wang, P. et al. Microecology in vitro model replicates the human skin microbiome interactions. *Nat. Commun.* **16**, 3085 (2025).
61. Dréno, B., Dagnelie, M. A., Khammari, A. & Corvec, S. The skin microbiome: a new actor in inflammatory acne. *Am. J. Clin. Dermatol* **21**, 18–24 (2020).
62. Lekbua, A. et al. SkinCom, a synthetic skin microbial community, enables reproducible investigations of the human skin microbiome. *Cell Rep Methods.* **4**, 100832 (2024).
63. Fyhrquist, N. et al. Microbe-host interplay in atopic dermatitis and psoriasis. *Nat. Commun.* **10**, 4703 (2019).
64. Yang, Z. et al. Nano-oxygenated hydrogels for locally and permeably hypoxia relieving to heal chronic wounds. *Biomaterials* **282**, 121401 (2022).
65. Greywal, T. et al. Evidence-based recommendations for the management of acne fulminans and its variants. *J. Am. Acad. Dermatol* **77**, 109–117 (2017).
66. Liu, X. et al. A tough, antibacterial and antioxidant hydrogel dressing accelerates wound healing and suppresses hypertrophic scar formation in infected wounds. *Bioact. Mater.* **34**, 269–281 (2024).
67. Peng, V. et al. Ornithine decarboxylase supports ILC3 responses in infectious and autoimmune colitis through positive regulation of IL-22 transcription. *Proc. Natl. Acad. Sci. USA* **119**, e2214900119 (2022).
68. Sajiir, H. et al. Harnessing IL-22 for metabolic health: promise and pitfalls. *Trends Mol. Med* **31**, 574–584 (2024).
69. Xu, Z. et al. Nanoparticles-incorporated hydrogel microneedle for biomedical applications: Fabrication strategies, emerging trends and future prospects. *Asian J. Pharm. Sci.* **20**, 101069 (2025).
70. González-Vázquez, P. et al. Transdermal delivery of gentamicin using dissolving microneedle arrays for potential treatment of neonatal sepsis. *J. Control Release* **265**, 30–40 (2017).
71. Ye, Y. et al. Apoptotic tumor DNA activated nanomotor chemotaxis. *Nano Lett.* **21**, 8086–8094 (2021).

Acknowledgements

This work was supported by National Key Research and Development Program of China (2022YFA1206900, Y.T.), and National Natural Science Foundation of China (22175083, Y.T. and 22375224, F.P.).

Author contributions

Z.H. and Y.G. contributed equally to this work. Z.H. and Y.T. participated in the conceptualization of the project. Z.H. and Y.S. were involved in the synthesis and characterization of nanomotors. Z.H., H.Q., and L.L. (Lu Liu) perform experiments in vitro. Z.H., Y.G., L.L. (Limeng Liu), and Z.F. contributed to the animal experiments. Z.H., Y.G. and Y.T. wrote the manuscript. Y.T., Z.F. and F.P. supervised the project.

Competing interests

The authors declare that they have no competing interests.

Additional information

Supplementary information The online version contains supplementary material available at https://doi.org/10.1038/s41467-026-68376-6.

Correspondence and requests for materials should be addressed to Fei Peng, Zhexiang Fan or Yingfeng Tu.

Peer review information *Nature Communications* thanks Tijana Miseljic, who co-reviewed with Ziqiao Li, Tzanko Tzanov, and the other, anonymous, reviewer(s) for their contribution to the peer review of this work. A peer review file is available.